1   [Short Title]: Extreme Geomagnetic Field Fluctuations

A Global Climatological Model of Extreme Geomagnetic Field Fluctuations

Neil C. Rogers*[1], James A. Wild[1], Emma F. Eastoe[1], Jesper W. Gjerloev[2], and Alan W. P. Thomson[3]

1.   Lancaster University, Lancaster, UK
2.   Johns Hopkins University – Applied Physics Laboratory, Laurel, MD, USA
3.   British Geological Survey, Edinburgh, UK

*Corresponding author: n.rogers1@lancaster.ac.uk

Abstract – This paper presents a multi-parameter global statistical model of extreme horizontal geomagnetic field fluctuations (dB_H/dt), which are a useful input to models assessing the risk of geomagnetically induced currents in ground infrastructure.   Generalised Pareto (GP) distributions were fitted to 1-minute measurements of $|dB_H/dt|$ from 125 magnetometers (with an average of 28 years of data per site) and return levels (RL) predicted for return periods (RP) between 5 and 500 years. Analytical functions characterise the profiles of maximum-likelihood GP model parameters and the derived RLs as a function of corrected geomagnetic latitude, λ. A sharp peak in both the GP shape parameter and the RLs is observed at $|\lambda| =53°$ in both hemispheres, indicating a sharp equatorward limit of the auroral electrojet region. RLs also increase strongly in the dayside region poleward of the polar cusp ($|\lambda|>75°$) for RPs > 100 years. We describe how the GP model may be further refined by modelling the probability of occurrences of $|dB_H/dt|$ exceeding the 99.97[th] percentile as a function of month, magnetic local time, and the direction of the field fluctuation, dB_H, and demonstrate that these patterns of occurrence align closely to known patterns of auroral substorm onsets, ULF Pc5 wave activity, and (storm) sudden commencement impacts. Changes in the occurrence probability profiles with the interplanetary magnetic field (IMF) orientation reveal further details of the nature of the ionospheric currents driving extreme $|dB_H/dt|$ fluctuations, such as the changing location of the polar cusp and seasonal variations explained by the Russell-McPherron effect.

1   Introduction

1.1   GICs and magneto-ionospheric currents

Large fluctuating magnetic fields arising from electrical currents in the ionosphere and magnetosphere can cause Geomagnetically Induced Currents (GICs) in any ground-based infrastructure that contains long metal conductors.   The damaging effects of GICs have been reported in relation to high voltage (HV) electricity power networks (Thomson et al. 2010; Boteler et al. 1998; Boteler & Pirjola 2017; Pirjola et al. 2000; Molinski, 2002; Erinmez et al. 2002), trans-oceanic cables (Lanzerotti et al. 1995; Root 1979), railway signalling systems (Wik et al. 2009; Eroshenko et al. 2010; Qian et al. 2016), railway electrification systems (Liu et al. 2016), and pipelines (Pulkkinen et al. 2001; Boteler 2000; Pirjola et al. 2000). In many cases, these systems need to be engineered with resilience to the potentially catastrophic GIC damage that occurs only rarely, which can be aided by an assessment of the likelihood of such events over a period of 100 years or more.

The magnitude of GICs in an electricity network is dependent on the geoelectric field, E, induced by a nearby ionospheric or magnetospheric current, and may be calculated using a grid model of electrical impedances and the application of Ohm's and Kirchhoff's laws, and Thévenin's theorem (e.g. Boteler & Pirjola 2014; 2017). Routine measurements of the geoelectric field are, however, not globally extensive and do not extend over the decades required for accurate climatological prediction of 1/100-year return levels. Instead, we have taken as a proxy the rate of change of the horizontal geomagnetic field dB_H/dt, which, when combined with a model of the local ground conductivity, may be used to predict E (Cagniard 1953). Digitised measurements of the geomagnetic field with 1-minute resolution are readily available and extend over several decades.

41 To simplify the calculation of E, it is often assumed that both geomagnetic and geoelectric field perturbations result from a
42 downward propagating plane wave and that the Earth conductivity is horizontally layered (see Pirjola 2002 for a review).
43 Under these assumptions the horizontal component of E follows the relation (Cagniard, 1953)

44
$$\begin{pmatrix} E_x \\ E_y \end{pmatrix} = \begin{bmatrix} Z_{xx}(\omega) & Z_{yx}(\omega) \\ Z_{xy}(\omega) & Z_{yy}(\omega) \end{bmatrix} \begin{pmatrix} dB_x/dt \\ dB_y/dt \end{pmatrix}$$

45 where the $Z_{ij}(\omega)$ are elements of a frequency-dependent impedance matrix which varies with location (x, y) if the local
46 geology is non-uniform.

47 An illustrative example of estimating GIC magnitudes from $|dB_H/dt|$ statistics was presented by Beggan et al. (2013). These
48 authors applied the 'thin-sheets' model of Vasseur & Weidelt (1977) to determine E at the Earth's surface based on the
49 (frequency-dependent) conductivity in the Earth crust in the United Kingdom. The magnetic field fluctuation was assumed
50 sinusoidal with a fixed period, and the root-mean-square rate-of-change dB_H/dt (required as an input to the model) was
51 taken from 100- and 200-year return value estimates from a study of European magnetometer records (Thomson et al. 2011).
52 The extreme geoelectric field estimates so produced were then input into a model of the UK high-voltage electricity grid to
53 determine the likely magnitude of GICs.   This calculation required an assumption of the principal direction for the field
54 fluctuation (e.g. North-South, or East-West) to drive various hypothetical scenarios.

55 In this paper we extend the statistics of the high percentiles and projected extreme values of $|dB_H/dt|$ to a full global extent
56 and provide a more detailed study of the direction of these fluctuations. We shall further show how the occurrence of
57 extreme $|dB_H/dt|$ (and hence GIC) at a given latitude may have limited extent in local time and their prevalence may be
58 confined to certain seasons – both factors that could be used to mitigate GIC risk. Fluctuation magnitudes of several hundred
59 nT/minute resulting from auroral current intensifications can cause HV electricity network outages, particularly if sustained
60 over a long duration (Knipp 2011, p.638–642; Erinmez et al. 2002) although other power grid impacts have been observed
61 at low- and mid-latitudes even for fluctuations less than 100 nT/minute (Kappenman 2006 and references therein; Gaunt
62 and Coetzee 2007; Trivedi et al. 2007).

63 The location and timing of large fluctuations of the magnetic field is, of course, dependent on the climatology of extreme
64 ionospheric and magnetospheric currents. The most intense GICs have been associated with intensifications of the Auroral
65 Electrojets (AEJ), which connect to the magnetosphere via the field-aligned Birkeland currents (Milan et al. 2017). These are
66 intensified during geomagnetically active periods such as substorms (e.g. Pulkkinen et al. 2003). The onset of auroral
67 substorms occurs preferentially in the 20–24 magnetic local time (MLT) sector (Liou et al. 2001; Wang et al. 2005) and is
68 followed by an expansion phase of about 25–40 minutes (Pothier et al. 2015) during which there are rapid intensifications
69 of the westward electrojet currents flowing along auroral arcs at the equatorward edge of the auroral region, which bulges
70 and expands poleward, eastward, and westward (Kivelson & Russell 2005, p.421–9; Gjerloev et al. 2007; Gjerloev & Hoffman
71 2013). The westward current enhancements are recorded as southward deflections of the magnetic field, as observed by
72 ground-based magnetometers. To a good approximation, the direction of any fluctuation, dB_H, measured at the ground is
73 90° anticlockwise from the ionospheric current direction (as viewed from above the current sheet) assuming planar
74 electromagnetic wave propagation and minimal horizontal gradients in ground conductivity (Viljanen et al. 2001;
75 Belakhovsky et al. 2019).

76 An illustrative example of substorm geomagnetic activity is presented in Figure 1a which presents the geomagnetic North
77 and East components of the magnetic field (the red and green lines, respectively) at the auroral magnetometer BRW
78 (Utqiagvik, Alaska, 70°N, 109°W in Corrected Geomagnetic (CGM) coordinates) and corresponding values for $|dB_H/dt|$ (blue
79 line), where exceedances of the 99.97-percentile ($P_{99.97}$) are highlighted in yellow. The strong southeast-directed fluctuation
80 dB_H at 07:07—07:10 UT could well have resulted from a strong southwest-directed electrojet current enhancement along
81 a brightening auroral arc during substorm expansion.
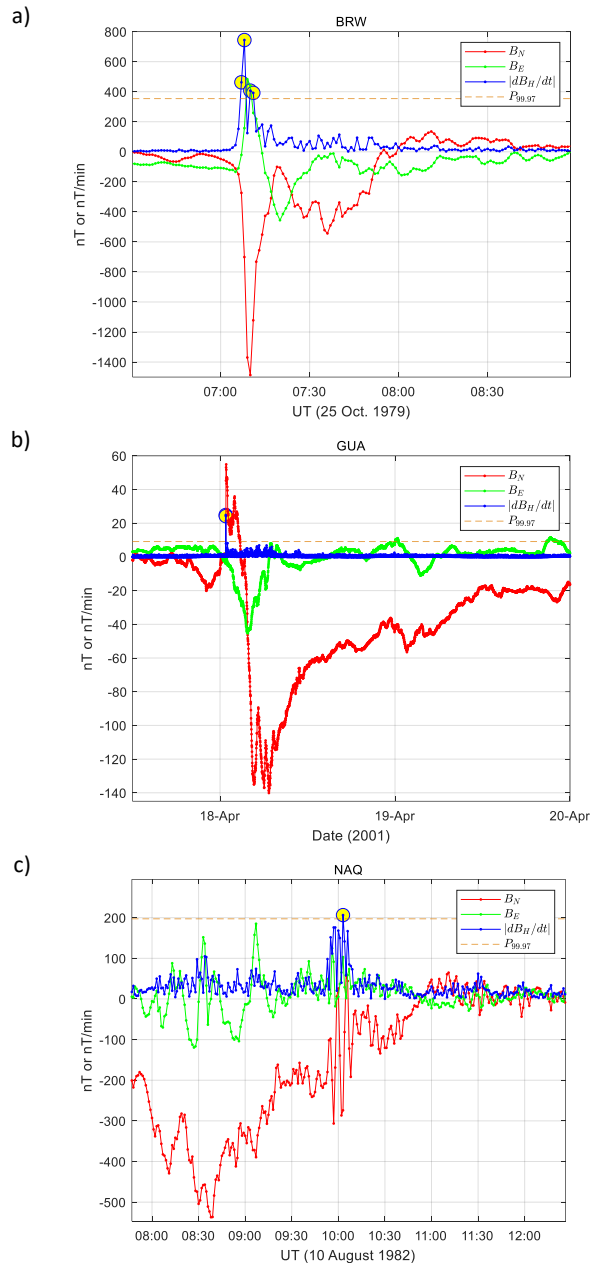
82   **Figure 1. Three examples of large field fluctuations $|dB_H/dt|$. a) An auroral substorm at BRW, Alaska, b) an SSC at GUA,**
83   **Guam, 6°N, 144°W CGM), and c) Pc5 pulsations (0945–1015 UT) at NAQ, Greenland. The 99.97th percentile of $|dB_H/dt|$ is**
84   **also shown.**

85   Strong "Region 0" (R0) currents may also flow along magnetic field lines into the polar cusp region, driven by magnetic
86   tension forces on field lines that have recently reconnected with the interplanetary magnetic field (IMF) at the dayside
87   magnetopause (Milan et al. 2017). The cusp lies poleward of the Birkeland currents, typically around 77–78° CGM latitude
88   and at 12 +/- 1.5 h MLT (p139, Campbell 2003; p237, Hunsucker and Hargreaves 2003), although under northward IMF
89   conditions it covers a wider latitude region extending to higher latitudes (Newell et al. 1989).   Large, transient (3–10-minute)
90   fluctuations of the vertical and horizontal geomagnetic field components have been observed for several decades at or just
91   equatorward of the cusp region (Sibeck 1993 and references therein). Many possible causes have been postulated, including
92   'flux transfer events' (Russell & Elphic 1978), enhanced dayside reconnection following a northward turning of the IMF (Pitout
93   et al. 2001), surface wave instabilities such as Kelvin-Helmholtz (K-H) waves (Masson & Nykyri 2018; Nykyri and Dimmock
94   2016), and solar wind plasma injections penetrating the magnetopause (Menietti & Burch 1988).

95   In many cases, there is a direct association between the high-latitude transients near the cusp region and geomagnetic storm
96   sudden commencements (SSC) and Sudden Impulses (SI) (Sibeck 1993; Sibeck & Korotova 1996; Lanzerotti et al. 1991). Figure
97   1b is the magnetogram from a low-latitude magnetometer (Guam) and includes a sharp increase in B_N at 00:47 UT on

98   28 April 2001 characteristic of an SSC. Sudden Commencements (SC) (a general term for both SSC and SI) occur in response
99   to step changes in solar wind dynamic pressure that cause a sudden increase in the Chapman-Ferraro current flowing
100 eastward along the dayside magnetopause boundary (Chapman & Ferraro 1931; Milan et al. 2017). They typically have a
101 magnitude of several tens of nT/minute at low latitudes, but may occasionally exceed 120 nT/min (Carter et al. 2015; Fiori
102 et al. 2014) and have been associated with GIC disturbances in HV electricity networks (Fiori et al. 2014; Kappenman 2003,
103 2004; Zhang et al. 2015; Marshall et al. 2012; Belakhovsky et al. 2017, 2019).

104 Other large fluctuations in B_H arise from intense ultra-low frequency (ULF) geomagnetic pulsations, the largest of which are
105 classed as 'Pc5 pulsations' with periods of 2.5 – 10 minutes (e.g. p168, Campbell 2003). Under typical mid-latitude conditions
106 and moderate geomagnetic activity, Pc5 waves have amplitudes of approximately 70 nT (p171, Campbell 2003). An example
107 of such waves is evident at 09:45–10:15 UT in the magnetogram for NAQ (Narssarssuaq, Greenland, 66.2°N, 42.5°E CGM)
108 presented in Figure 1c. The most powerful Pc5 pulsations are observed in the period between dawn and noon, and can arise
109 from an Alfvén wave K-H instability, particularly during periods of high velocity solar wind (>500 km s^{-1}) (Engebretson et al.
110 1998; Pahud et al. 2009; Vennerstrøm 1999). Alternatively, Pc5 waves may be triggered by shocks in the solar wind
111 associated with Sudden Commencements (Zhang et al. 2010; Hao et al. 2019; Zong et al. 2009).

112 Belakhovsky et al. (2019) also recently considered the importance of irregular Pi3 ULF waves and Travelling Convection
113 Vortices (TCV) in driving large $|dB_H/dt|$ events. Pi3 waves are described as "quasi-periodic sequences of magnetic impulses"
114 with timescales between 10 and 20 minutes, and TCVs have been observed as a twin vortex of Hall currents in the polar cleft
115 region. TCVs are generated by a pair of upward and downward field-aligned currents that can be triggered by a sudden
116 change in the solar wind (Engebretson et al. 2013; Friis-Christensen et al. 1988; Vorobjev et al. 1999).

1.2   Modelling the probability of extreme field fluctuations

118 The probability distribution of non-extreme values of $|dB_H/dt|$ at any given location is well approximated by a lognormal
119 distribution (Manpreet 2018; Love et al. 2016). This distribution may not be suitable for extremes since its purpose is to
120 produce a good fit to the main body of the distribution rather than the tails, and it may not extrapolate well beyond the
121 observed range of the data.   Because extreme events are, by definition, rare, there is little evidence from the data with
122 which to validate the appropriateness of the fit of a lognormal to the tail.

123 To model the tail distribution, extreme value theory (EVT) has been applied (Coles 2001; Reiss & Thomas 2007) and a
124 Generalised Pareto (GP) distribution fitted to observations of $|dB_H/dt|$ above a high threshold. By modelling how the site-
125 specific parameters of the GP distributions vary globally, we shall present model-based predictions of the 'return value' of
126 $|dB_H/dt|$ at any location on the Earth for 'return periods' ranging from 5 to 500 years. We have also examined the
127 probability of $|dB_H/dt|$ threshold exceedances as a function of month, MLT, and the direction of the fluctuation, $\mathbf{dB_H}$. This
128 additional information helps to associate extreme magnetic field fluctuations with their causative extreme ionospheric and
129 magnetospheric electrical currents. Modelling patterns of occurrence probability in this way also improves the modelling of
130 risk when engineering GIC resilient ground infrastructure, noting that electricity usage or signalling error requirements may
131 vary with time-of-day and season (e.g. Molinski 2002). Individual linear elements of pipelines or electricity cables are also
132 sensitive to fluctuations resolved along only one directional axis.

133 In previous studies, EVT has been used to examine the likelihood of extreme values of geomagnetic indices including D_{st}
134 (Tsubouchi & Omura 2007; Silbergleit 1996), the Auroral Electrojet indices (AU, AL and AE) (Nakamura et al. 2015), A_p (Koons
135 2001), and the *aa* and *AA** indices (Silbergleit 1999; Siscoe 1976), although the location and timing of large $|dB_H/dt|$ events
136 are not well predicted by geomagnetic index statistics (e.g. Kozyreva et al. 2018).   In related space weather fields, EVT has
137 characterised the probability of extreme solar flare X-ray flux (Elvidge & Angling 2018; Tsiftsi & De La Luz 2018) and extreme
138 high-energy (> 2 MeV) radiation-belt "killer" electron fluxes (Koons 2001; O'Brien et al. 2007; Meredith et al. 2015).

139 EVT and other statistical approaches have been applied to the prediction of extreme $|dB_H/dt|$ in several previous
140 publications (Thomson et al. 2011; Wintoft et al. 2016; Love et al. 2016; Nikitina et al. 2016) and individual case studies have
141 examined extreme $|dB_H/dt|$ characteristics (e.g. Pulkkinen et al. 2012; Viljanen et al. 2001; Ngwira et al. 2013, Kozyreva et
142 al. 2018). In Section 3 of this paper, we present a new assessment based on a significantly larger dataset than presented in
143 these earlier studies – 1.9 billion field measurements from 125 magnetometers worldwide. This is followed by an analysis
144 of the latitudinal, seasonal, MLT, and directional dependences of the extreme events, presented as occurrence probability
145 distributions for $|dB_H/dt|$ exceeding the 99.97th percentile ($P_{99.97}$). In Section 4 (Discussion) we shall (i) relate our new
146 findings to the earlier studies cited above, (ii) further assess the importance of SC in triggering impulses at high latitudes, and

147   (iii) show how the occurrence probability profiles change with IMF orientation. The paper concludes with a summary of these
148   findings.

2   Data and Methods

2.1   Magnetograms

151   The magnetic field measurements for this study were obtained through SuperMAG, an interface to magnetic measurements
152   made by a global network of geophysical institutes; SuperMAG being a project led by Johns Hopkins University (Gjerloev
153   2009). Gjerloev (2012) described the processing of the magnetometer measurements in the SuperMAG data set which may
154   be summarised as follows: The field measurements (1-minute averages) were rotated into a local NEZ geomagnetic
155   coordinate system (N = north, E= east, Z = down) using a time-dependent local declination angle obtained using a 17-day
156   sliding window smoothing filter. For each magnetometer, the N, E and Z components were then individually baselined as
157   follows: (i) Diurnal variations of the field (mainly due to the S_q current system: Matsushita (1968); Yamazaki (2017)) were
158   removed by subtracting a diurnal trend, (ii) the secular variation of the Earth's main field was removed by subtracting the
159   linear trend over each year (with some contribution from neighbouring years), and (iii) the residual scalar offset was
160   subtracted. This method of processing preserves the short-term field fluctuations associated with substorms, as well as
161   those due to geomagnetic storms. Long-period (>1 month) variations in the declination angle are, however, removed by the
162   rotation into local NEZ coordinates.
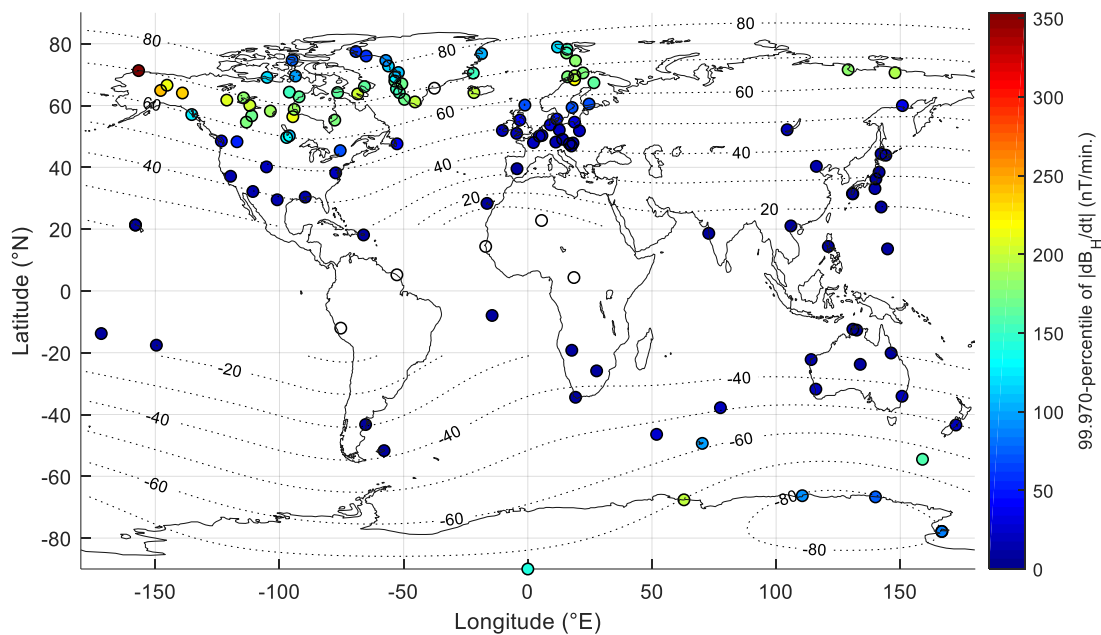
Figure 2. Magnetometer sites in the SuperMAG collaboration with ≥ 20 years data, coloured by $P_{99.97}$ at each site. Contours show CGM latitudes for IGRF model epoch 2000.

163
164   The magnetometer records in the SuperMAG archive had already been cleaned and manually inspected to remove most
165   sudden changes in the baseline (offsets), spikes, and gradual slopes (Gjerloev 2012). However, for this study – since the
166   statistics of extreme and rare events may be significantly influenced by a small number of imperfections – all the data in
167   weeks containing $|dB_H/dt|$ peaks above the 99.97th percentile ($P_{99.97}$) were further visually inspected and obvious artefacts
168   replaced by data gaps. Examples of common artefacts requiring correction were: (i) large, isolated, 1–2 minute-duration
169   spikes in signal levels (B_N and/or B_E), (ii) large step-changes in signal level, often occurring at the 00:00 UT boundary and
170   sometimes followed by a correction to previous levels after an interval of perhaps 30–60 minutes, (iii) an obvious saturation
171   in signal level, which occurred for $B_N \approx$ -1000 nT at several auroral magnetometers on several occasions.

172 In relation to GICs, the North and East components of the induced geoelectric field are approximately proportional to
173 (Wintoft et al. 2016)

174 $$(E_N, E_E) = k \left(\frac{dB_E}{dt}, \quad -\frac{dB_N}{dt} \right)$$

175   (1)

176 where B_N and B_E are the Northward and Eastward components of the geomagnetic field and k is a constant that depends
177 on the local ground conductivity. Equation (1) is valid under the assumptions that the magnetic disturbance propagates as
178 a plane wave and the ground conductivity has no horizontal gradients. We therefore define $|dB_H/dt|$ as

179 $$\left| \frac{dB_H}{dt} \right| = \frac{1}{\Delta t} \sqrt{(\Delta B_N)^2 + (\Delta B_E)^2}$$

180   (2)

181 where $\Delta B_N = B_N(t + \Delta t) - B_N(t)$ and $\Delta B_E = B_E(t + \Delta t) - B_E(t)$. This definition (which was also adopted by Wintoft et
182 al. 2015, 2016; Ngwira et al. 2018; Falayi et al. 2017; Kozyreva et al. 2018 and others) ensures that statistics of the induced
183 E-field magnitude, $|E| = \sqrt{E_N^2 + E_E^2}$ required for GIC modelling will be directly proportional to the distribution of $|dB_H/dt|$
184 given by Equation (2). The compass *direction* of $\boldsymbol{dB_H}/dt$ was also recorded as

185 $$D = \arg(\Delta B_N + \mathrm{i}\, \Delta B_E)$$

186   (3)

187 There are 130 magnetometer sites in the SuperMAG database for which at least 20 years of data were available. These
188 covered the period from 1-Jan-1969 to 31-Dec-2016 (albeit with some data gaps). Five stations at low-latitude locations in
189 the Atlantic longitude sector (HUA, BNG, KOU, MBO, and TAM, shown unshaded in Figure 2) were excluded from analysis
190 since their locations in the corrected geomagnetic (CGM) coordinate system are undefined (see Fig. 7 of (Laundal & Richmond
191 2017)). Average geomagnetic CGM coordinates were calculated using the software described by Shepherd (2014) and are
192 listed together with site codes, names, and geodetic coordinates in Supplementary Material (folder S1). Figure 2 presents a
193 map of these locations with colours representing $P_{99.97}$. Immediately apparent from Figure 2 is the maximum in $P_{99.97}$ in the
194 auroral zones (approximately 55–75° CGM latitude) in both hemispheres, although the density of sites is much greater in the
195 northern hemisphere.

2.2   Fitting the GP tail distribution

197 Taking a sequence of independent and identically distributed (IID) random variables, $\boldsymbol{x} = [x_1, x_2, \ldots, x_n]$, and a sufficiently
198 high threshold, u, it may be shown that the cumulative distribution function of threshold exceedances $\boldsymbol{y} = \boldsymbol{x} - u$, conditional
199 on $\boldsymbol{x} > u$, takes the approximate form of a Generalised Pareto (GP) distribution (Coles 2001, p.75) given by

200 $$H(\boldsymbol{y}) = 1 - \left(1 + \frac{\xi \boldsymbol{y}}{\sigma} \right)^{-\frac{1}{\xi}}$$

201 defined on $\{\boldsymbol{y}: \boldsymbol{y} > 0 \text{ and } (1 + \xi \boldsymbol{y}/\sigma) > 0\}$, where $\sigma > 0$ is the scale parameter, and ξ the shape parameter of the
202 distribution. Note that in the limiting case $\xi \to 0$, $H(\boldsymbol{y}) \to 1 - \exp(-\boldsymbol{y}/\sigma)$, that is, the distribution of $\boldsymbol{y}$ is exponential.
203 Where $\xi < 0$, the distribution is bounded to an upper limit of $u - \sigma/\xi$, whilst if $\xi > 0$ the distribution is heavy-tailed, with
204 no upper limit. The occurrence probability of extreme $\boldsymbol{x}$ therefore increases with ξ and/or σ.

205 Because the above model is based on an asymptotic result that only holds exactly as $u \to y_+$, where

206 $$y_+ = \min\{\boldsymbol{y}: H(\boldsymbol{y}) = 1\}$$

207 is the upper end-point of the distribution of $\boldsymbol{y}$, the threshold u must be set high enough that the approximation for finite u
208 can be assumed to be valid, i.e. so the distribution fits the observed threshold exceedances well. Conversely, u should not
209 be so high that the sample size for modelling is too small. A 99.97-percentile threshold was adopted in this study following
210 the assessment of Thomson et al. (2011) based on 28 European magnetometers, and the case study of Nikitina et al. (2016)
211 who suggested thresholds in the region 99.93–99.97% for the site VIC (Victoria, Canada). Based on the assumption that

212   threshold exceedances are a set of independent observations drawn from a GP distribution with common parameters (σ, ξ),
213   these parameters can be estimated by maximisation of an appropriate likelihood function (Pawitan 2001).

214   Occurrences of peaks over the threshold ($|dB_H/dt| > u$) often exhibit short-range temporal dependence, with tight
215   clustering of peaks (e.g. during a geomagnetic storm). This violates the assumption of an IID random sequence required in
216   fitting the GP distribution as described above. The easiest way to deal with this is to ensure temporal independence by
217   extracting independent clusters of extreme events and modelling only the maxima of these clusters. Consequently, the
218    $|dB_H/dt|$ data were declustered using a 'run-length below threshold' method such that any exceedances of $P_{99.97}$ within 12
219   hours of the previous exceedance were considered to be part of the same cluster, and only the largest $|dB_H/dt|$ in each
220   cluster was recorded. Thomson et al. (2011) discussed the merits of alternative declustering thresholds and run lengths, but
221   concluded that the 99.97th percentile and 12-hour run-length were a reasonable compromise.

222   A measure of the short-range temporal dependence in the peaks ($\left|\frac{dB_H}{dt}\right| > u$), called the 'extremal index', was empirically
223   determined as (p.103, Coles, 2001)

224
$$\hat{\theta} = n_c / n_u$$

225   where n_c is the total number of clusters, and n_u is the total number of peaks above the high threshold, u. The index $\hat{\theta}$ may
226   be interpreted loosely as the reciprocal of the mean number of peaks in each cluster.

227   The maximum likelihood estimates (MLE) of GP parameters ξ and σ at each site were determined, together with 95%
228   confidence intervals (CI) based on the asymmetric likelihood profiles. Following (Coles 2001, p.78*ff*) diagnostic tests were
229   then conducted to ensure that if the threshold were to be increased to u^* (for all $u^* > u$) then both the shape, ξ, and the
230   'modified scale', $\sigma^* = \sigma - \xi u^*$, would remain constant, and the mean excess of the tail distribution, $E(x - u^* \mid x > u^*)$,
231   would scale in proportion to u^*, as required. The empirical and model tail distribution functions were then visually compared
232   to ensure that the model was a good fit to the measurements at the new 'manually revised' threshold.

233   The *m*-observation return level, x_m (nT/minute) was calculated from MLE GP parameters as (Coles 2001, p.103)

234
$$x_m = u + \frac{\sigma}{\xi}\left[\left(m\hat{\theta}\hat{\zeta}_u\right)^{\xi} - 1\right]$$

235   (4)

236   where $\hat{\zeta}_u$ is the probability of threshold exceedance, determined empirically as

237
$$\hat{\zeta}_u = \frac{n_u}{n}$$

238   and n is the total number of measurements. As an example, for a 100-year return period and 1-minute measurements
239   setting $m = 100 \times 365.25 \times 24 \times 60 = 52{,}596{,}000$ in Equation (4) yields the 100-year return level.

240   For each cluster peak ($|dB_H/dt| > u$) we recorded the magnetic local time (MLT), defined as (Laundal & Richmond 2017)

241
$$MLT = \frac{\left(\phi - \phi_{cd,ss}\right)}{15°} + 12$$

242   where $\phi_{cd,ss}$ is the centred dipole longitude of the sub-solar point, in degrees, (determined using the formulas in Appendix C
243   of (Laundal & Richmond 2017)) and ϕ is the geomagnetic longitude of a magnetometer in CGM coordinates. $\phi_{cd,ss}$ was
244   determined as

245
$$\phi_{cd,ss} = \Phi_{geo,ss} - \Phi_N$$

246   where $\Phi_{geo,ss}$ is the geographic longitude of the sub-solar point and Φ_N is the centred dipole longitude of the North Pole,
247   determined as

248
$$\Phi_N = \arg(-g_1^1 - ih_1^1)$$

249   where g_1^1, h_1^1 are Gauss coefficients of the International Geomagnetic Reference Field (IGRF) (Thébault et al. 2015), linearly
250   interpolated in time. The CGM longitude, ϕ, was determined for each site at 1-year intervals using the software described
251   by Shepherd (2014) and then linearly interpolated onto a 1-minute-resolution time scale.

252   IMF components B_y (duskward) and B_z (northward) were also recorded in geocentric solar magnetic (GSM) coordinates
253   (Laundal & Richmond 2017) for each cluster peak. The IMF measurements were interpolated from 1-hour average values
254   provided in the NASA Goddard Space Flight Center's "OMNI" database (https://omniweb.gsfc.nasa.gov). These
255   measurements from spacecraft at the L_1 Lagrange point have been time-shifted to account for the propagation delay to the
256   magnetospheric bow shock nose using the method of Weimer et al. (2003).

3   Results

257

3.1   Latitudinal profiles of extreme $|dB_H/dt|$

258

259   Figure 3a presents $P_{99.97}$ for the 1-minute $|dB_H/dt|$ as a function of the mean absolute CGM latitude, $|\lambda|$, for each
260   magnetometer site (the mean is presented since the latitude can vary a few degrees over the period of measurements). The
261   blue crosses in Figure 3a represent $P_{99.97}$, whilst the red circles indicate the manually revised thresholds, following the
262   diagnostic tests described above. The outlier at λ = 70°N is for the site at Utqiagvik, (formerly Barrow), Alaska (BRW), which
263   together with nearby sites in Alaska presents anomalously high values for $|dB_H/dt|$ (Figure 2). Viljanen et al. (2001)
264   speculated that local anomalies in the strength and direction of the fluctuations (as observed at four out of 25
265   magnetometers in Fennoscandia) could result from regions of anomalously high conductivity in the Earth's crust since telluric
266   currents induced in the crust contribute to the measurement of dB_H/dt at the magnetometer. Kozyreva et al. (2018, p.10)
267   also noted that coastal stations BRW and AND produced anomalously high $|dB_H/dt|$ during the intense March 17, 2015
268   geomagnetic storm. Measurements from these magnetometer sites have, however, been retained in the analysis to avoid
269   any subjective bias in the selection of data.

270   The MLEs for the fitted scale and shape parameters are presented in Figure 3b and c respectively, with error bars
271   representing the 95% confidence intervals. Northern hemisphere (NH) stations are presented in black and southern
272   hemisphere (SH) stations in blue, showing that there are no significant hemispherical differences in the CGM latitude profiles.
273   There is a substantial difference in the functional form between the scale, $\sigma(|\lambda|)$, and the threshold, $u(|\lambda|)$: There is a
274   positive skew in $\sigma(|\lambda|)$ that is not apparent in $u(|\lambda|)$, which is more evenly distributed about 67°. Similarly, the functional
275   form of the shape parameter profile, $\xi(|\lambda|)$, (Figure 3c) exhibits a sharp peak at 53° CGM latitude, a broad minimum in the
276   auroral zone (centred about 70°) and a clear increase in value towards the geomagnetic poles. The extremal index, $\hat{\theta}$,
277   presented in Figure 3d indicates strong latitudinal variation in the level of short-range temporal dependence (or level of
278   clustering). Figure 3e presents the number of measurements for each site (approximately 10-25 million), the number for
279   which $|dB_H/dt|$ exceeded $P_{99.97}$, and the number of clusters for each site (from 146 to 1084), and the mean number of
280   clusters per year of data (from 5 to 56).

281   The MLE parameters presented in Figure 3 were substituted into (4) to determine the MLE values of return levels presented
282   for each site in Figure 4. The sharp rise in return level at latitudes near $|\lambda|$ = 53°, typically considered to be sub-auroral under
283   quiet to moderate geomagnetic conditions, arises from large values of both the σ and ξ parameters at this latitude.
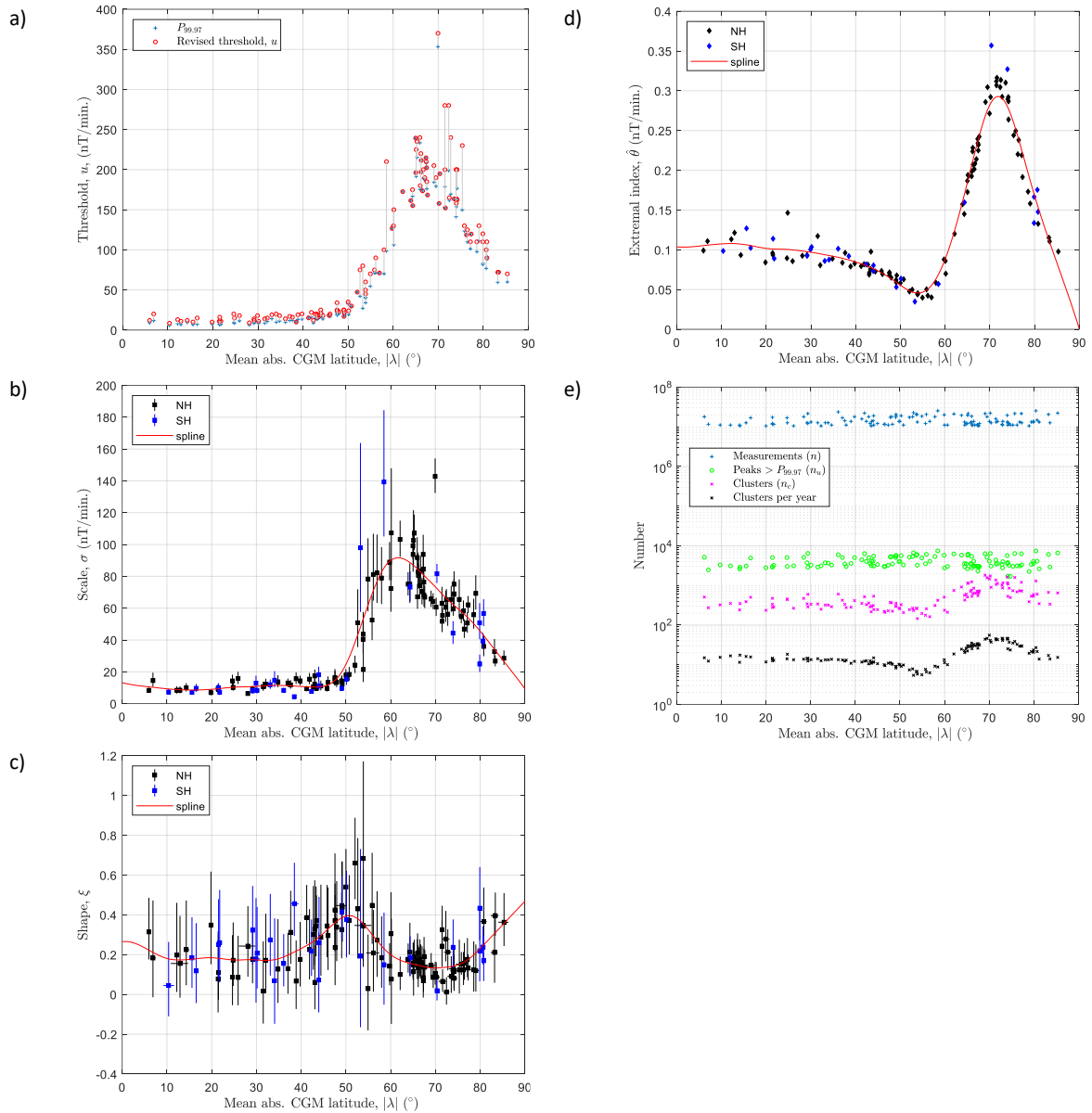
Figure 3. GP parameters for 125 magnetometers *vs.* absolute CGM latitude. a) 99.97-percentiles of $|dB_H/dt|$ and revised thresholds, u, b) MLEs of scale, σ (error bars indicate 95% CIs), c) MLEs of shape, ξ, d) extremal index, $\widehat{\theta}$, e) number of measurements, n, number exceeding $P_{99.97}$, n_u, number of clusters, n_c, and mean n_c per year. Red curves indicate fitted smoothed splines (5).
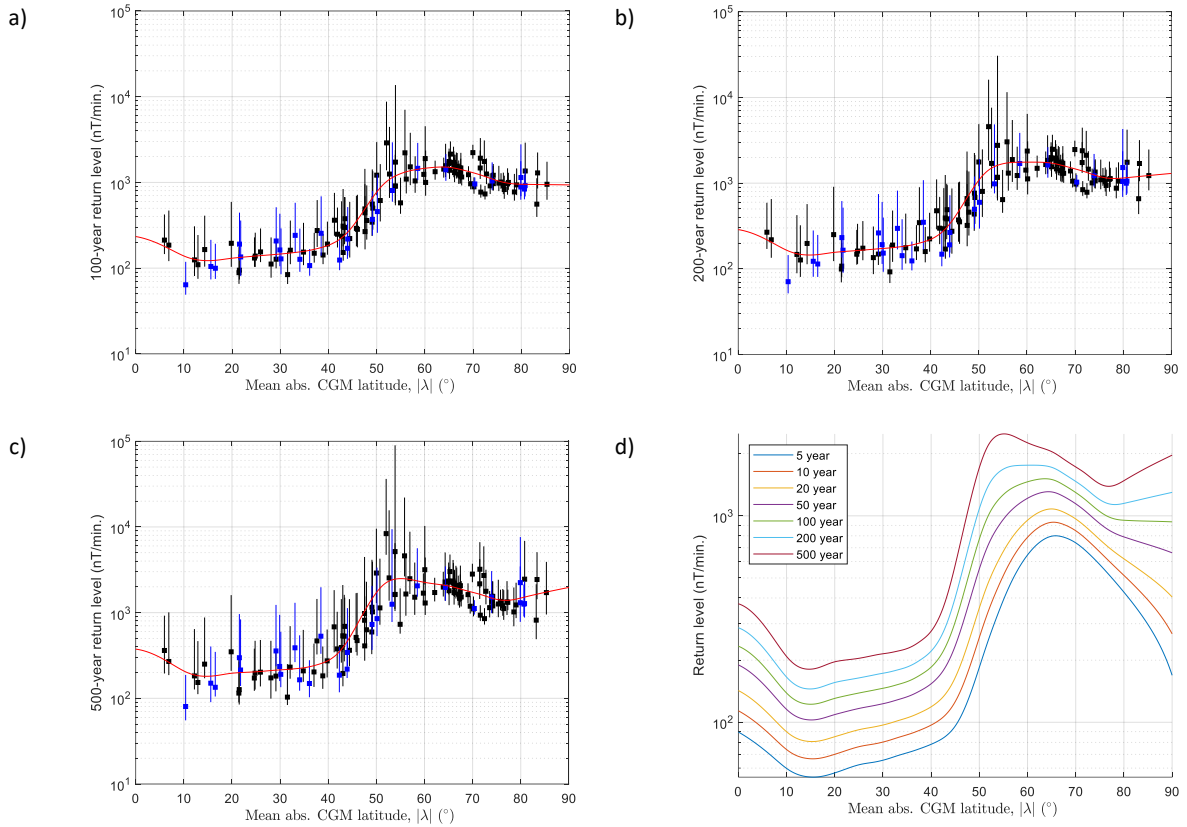
288 **Figure 4. Return levels of $|dB_H/dt|$ (MLEs, with 95% Cis shown as error bars), for return periods of a) 100 years, b) 200**
289 **years, and c) 500 years with fitted smoothed splines ($s(|\lambda|)$ in (5)). Panel d) shows spline fits for a range of return periods.**

290 The curves in Figure 3 and Figure 4 represent smoothing spline functions, s, found by minimising

$$p \sum_i \left(z_i - s(|\lambda_i|)\right)^2 + (1-p) \int \left(\frac{d^2 s}{d\lambda^2}\right)^2 d|\lambda|$$

292   (5)

293 where z_i are the ordinates (e.g. the MLE GP parameter at each site, i), and p is a smoothing parameter. The choice of p =
294 0.01 provided a good balance between goodness of fit (the first term in (5)) and function smoothness (the second term of
295 (5)). The numerical minimisation algorithm used was based on the MATLAB™ function *csaps*. A MATLAB™ script to
296 regenerate all of the spline curves of Figure 3 and Figure 4 is provided in Supplementary Material (folder S2).

297

298   3.2   Probability of occurrence *vs* latitude and MLT

299 When modelling return levels, the probability of threshold exceedance $\hat{\zeta}_u$ in (4) may be modelled as a function of observed
300 covariates, i.e. $\hat{\zeta}_u = \hat{\zeta}_u(\alpha_1, \alpha_2, \dots)$, where α_i are site-specific, possibly time-varying, covariates of the data (e.g. MLT, month,
301 direction, etc.). This additional information allows a prediction of GIC risk to be refined for systems operating in a restricted
302 range of local times, times of year, etc., or for individual elements of pipeline or cable network with a fixed directional
303 orientation. The latitudinal, seasonal and diurnal patterns in the occurrences of $|dB_H/dt|$ exceeding $P_{99.97}$ may be used as
304 an approximation to $1 - \hat{\zeta}_u(\alpha_1, \alpha_2, \dots)$ for $u \approx P_{99.97}$, and these patterns are also useful in identifying the general
305 ionospheric/magnetospheric current systems driving the extreme geomagnetic fluctuations.

306 Figure 5a presents the number of cluster peaks for all magnetometers, binned by $|\lambda|$ and MLT, i.e.

307

308
$$N(|\lambda|, MLT) = \sum_s n_{c,s}(|\lambda|, MLT)$$

309 where $n_{c,s}(|\lambda|, MLT)$ is the number of cluster peaks in each ($|\lambda|$, MLT) bin for site s (latitude bins containing no
310 magnetometers are shown in grey). The summation of cluster peaks over multiple sites has the effect of smoothing the
311 distribution and reducing quantisation noise where $n_{c,s}(|\lambda|, MLT)$ may be small. Since the number of magnetometer
312 measurements varies with latitude, Figure 5b re-presents the same data after normalisation by the number of cluster peaks
313 recorded in each bin. This is a close approximation to the 2-d distribution of occurrence likelihood for cluster peaks exceeding
314 $P_{99.97}$ and it was calculated as

315
$$P(|\lambda|, MLT) = \frac{N(|\lambda|, MLT)}{\sum_S n_{c,s}(|\lambda|)} \times \frac{\Delta\lambda}{90°}$$

316 where $n_{c,s}(|\lambda|)$ is the total number of cluster peaks for a site s that lies within the latitude bin of width $\Delta\lambda$, and we have
317 assumed the observations are uniformly distributed in MLT. Note that, where $\Delta\lambda$ is chosen to prevent data gaps,

318
$$\sum_{|\lambda|} \sum_{MLT} P(|\lambda|, MLT) = 1$$

319 Figure 5b shows that at auroral latitudes (55–80° CGM) the cluster peaks occur most often at 20–24 MLT, which is the time
320 sector associated with the greatest number of substorm onsets. A cursory inspection of magnetometer records associated
321 with these peaks indicated that many were indeed associated with substorm activity (similar to that in Figure 1a).

322 The second most prominent region of high occurrence is at 10–14 MLT above 77° CGM latitude, i.e. the region poleward of
323 the dayside cusp. It should be emphasised that since Figure 5 relates to percentiles $P_{99.97}$ that are themselves a function of
324 $|\lambda|$ (as presented in Figure 3a) the magnitudes of the $|dB_H/dt|$ peaks in this high-latitude region are much lower than in the
325 auroral and sub-auroral zones.   Nonetheless, the clustering of events about 12 MLT is very clear.

326 A third region of raised occurrence likelihood is observed in Figure 5b with a well-defined increase in the MLT locus of cluster
327 peaks from 3 to 10 MLT as CGM latitude increases from 60° to 75°. This pattern aligns with patterns of Pc5 wave occurrence
328 reported in the literature: For example, Baker et al. (2003) observed an increase in Pc5 wave power from 7 to 9 MLT as λ
329 increased from $65 - 74°$N, Pahud et al. (2009) showed Pc5 power upper quartiles increasing from 4 to 8 MLT between 61–
330 69°N CGM under conditions of high solar wind speed, and the average wave power distributions in Fig. 5 of Vennerstrøm
331 (1999) show a clear pattern of wave power increasing from approximately 67° to 75°N invariant latitude over the 4–12 MLT
332 range with a secondary maximum around local midnight (22–2 MLT) attributed to substorms. The effect was also noted in
333 $|dB_H/dt|$ measurements by Viljanen et al. (2001) for three sites in Scandinavia. Various theories for the asymmetry in Pc5
334 wave activity about local noon were discussed by Pahud et al. (2009, and references therein) and include a dawn-dusk
335 asymmetry in the wave excitation processes in the magnetosphere, differences in the harmonic modes and polarisations of
336 the waves, and differences in the level of screening by the conductive ionospheric layer.
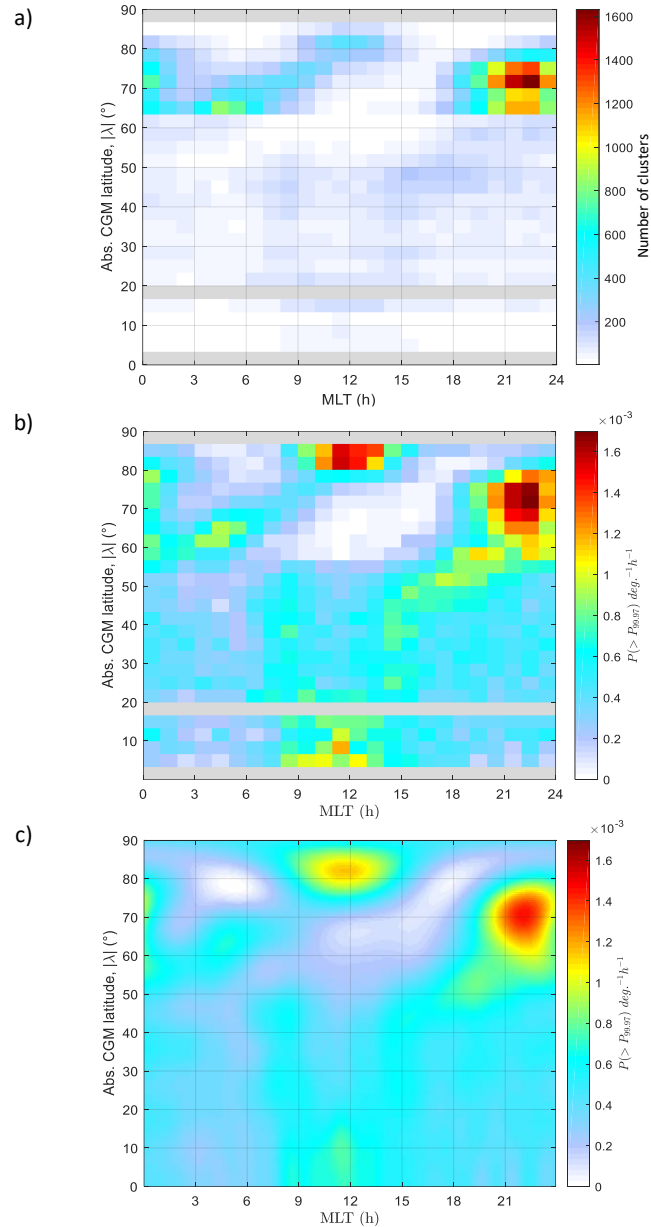
337 **Figure 5. Total occurrences of cluster peaks binned by geomagnetic latitude $|\lambda|$ and MLT. a) Number of clusters, b)**
338 **probability distribution of cluster peaks, c) fitted spherical harmonic expansion (P_{sph} in (6)).**

339 At latitudes below 50° CGM, there is a distribution of cluster peaks between 6 and 18 MLT forming a V-shaped distribution
340 centred about 11 MLT, with a reduced spread of local times at the lowest latitudes. This is broadly consistent with
341 enhancement in SC amplitudes between 08 and 16 MLT (maximising at 11 MLT) near the equator reported by Shinbori et al.
342 (2009), Russell et al. (1994) and others. These authors also reported a broad enhancement in SC amplitude in the midnight
343 sector attributed to strong cross-magnetotail and field-aligned currents, but no enhancement of midnight sector cluster peak
344 frequency is evident in Figure 5 indicating that most $|dB_H/dt|$ cluster peaks in this local time sector have magnitudes below
345 the 99.97th percentile. Further investigations are required to identify the physical processes associated with the V-shaped
346 occurrence distribution, which has maxima at approximately 08 and 15 MLT for absolute CGM latitudes between 20° and
347 40°.

348 The empirical data values from Figure 5b could be applied directly in a model of $1 - \widehat{\zeta}_u(|\lambda|, MLT)$ with interpolation and
349 extrapolation in regions of missing data. As an alternative, a 2-d spherical harmonic series expansion has been fitted to the
350 data producing the smooth model surface shown in Figure 5c. The spherical harmonic expansion (6) was fitted by regression
351 to $P(|\lambda|, MLT)$ and normalised to ensure a non-negative model probability distribution that integrated to unity:

352
$$P_{sph}(\lambda, MLT) = \sum_{l=0}^{L} \sum_{m=-l}^{l} A_{lm} P_l^m(\sin \lambda) \, e^{im\pi MLT/12}$$

353   (6)

354   where P_l^m are Schmidt semi-normalized associated Legendre polynomials, and MLT is in hours. A minimum order of L=19

355   was required to adequately represent the structure in distribution. The 400 complex A_{lm} coefficients are provided as

356   Supplementary Material (folder S3), together with example MATLAB™ code to reproduce $P_{sph}(\lambda, MLT)$.

3.3   Seasonal, MLT, and directional distributions

358   The patterns of cluster peaks with month and MLT are presented in Figure 6. Each panel presents, using a subset of

359   magnetometer sites in a particular band of CGM latitudes, the distribution

360
$$P(month, MLT) = \frac{\sum_s n_{c,s}(month, MLT)}{\sum_s n_{c,s}}$$

361   where $n_{c,s}(month, MLT)$ is the number of cluster peaks in each (month, MLT) bin for site s, and $n_{c,s}$ is the total number of

362   clusters for site s. Since the number of field measurements in each (month, MLT) bin is approximately equal, the

363   value $P(month, MLT)$ approximates the 2-d probability distribution of cluster peak occurrences. Figure 7 presents, in a

364   similar format to Figure 6, the distribution

365
$$P(D, MLT) = \frac{\sum_s n_{c,s}(D, MLT)}{\sum_s n_{c,s}}$$

366   where D is the compass direction of the large geomagnetic fluctuation (3). Note in each case that

367
$$\sum_{month} \sum_{MLT} P(month, MLT) = \sum_{D} \sum_{MLT} P(D, MLT) = 1.$$

368   Panels $a - c$ in Figure 6 and Figure 7 present the occurrence distribution for NH magnetometer sites ($\lambda > 0$), whilst panels

369    $d - f$ are for SH sites ($\lambda < 0$). Panels a and d in both figures were produced from a subset of low latitude sites ($|\lambda| < 40°$) and

370   display a slight increase in occurrence likelihood on the day side, between 7 and 17 MLT, with little seasonal variation. The

371   associated direction distribution in Figure 7 a and d shows a strong 'preferred direction' for these large events, principally

372   towards the north ($D \approx 0°$) at most times of day, with a secondary maximum for southward fluctuations ($D \approx 180°$). A large

373   proportion of the events are associated with SC, which is characterised by a large northward-directed dB_H impulse.

374   However, in the 6–10 MLT region, the directional distribution $P(D, MLT)$ is more isotropic. Repeating the analysis with no

375   declustering produces very similar distributions for $P(D, MLT)$ (not shown), albeit with less quantisation noise. This indicates

376   that the choice of declustering parameters does not affect $P(D, MLT)$ substantially.

377   Panels b and e of Figure 6 represent a subset of stations in a band of auroral latitudes (55 < $|\lambda|$ < 75°) and present a marked

378   increase in the rate of occurrence in the pre-midnight hours (20–24 MLT) maximising near the equinoxes, with a secondary

379   maximum in the winter months centred approximately one hour later at 22–24 MLT. This is consistent with the 1-hour

380   difference in substorm onset MLTs between summer and winter reported by Liou et al. (2001). Geomagnetic activity is

381   generally increased near the equinoxes when the geomagnetic field is more favourably oriented for reconnection with the

382   IMF (Russell & McPherron 1973; Zhao & Zong 2012) and this effect has been observed in several previous studies of

383   geomagnetic fluctuations (Viljanen et al. 2001; Beamish et al. 2002; Boteler et al. 1998). The same panels in Figure 7 show

384   that the principal direction of the dB_H in this MLT sector is southward ($D \approx 180°$), which indicates that strong westward

385   auroral electrojet currents are the dominant driver of such fluctuations.

386   The period 3–11 MLT in Figure 6 (b and e) is also associated with raised occurrence probability and follows the known

387   patterns of enhanced ULF wave activity described in Section 3.2. In the NH (Figure 6b) the region of higher occurrence

388   likelihood is centred at approximately 4 MLT near the June solstice but increases to 9 MLT towards the December solstice.

389   The seasonal pattern in the southern hemisphere is less clear due to the smaller number of observations in this region. The

390   corresponding panels of Figure 7 show that the direction of these changes in the NH is broadly aligned to the axis ESE – WNW

391   (100° – 280°) from 3–7 MLT, but move closer to the N–S axis for events near the December solstice at MLT 7–11. Again the

392   trends in the Southern hemisphere are less clear due in part to the smaller number of magnetometer stations.

393   Panels c and f in Figure 6 were produced from the subset of magnetometers with $|\lambda| > 77°$ (i.e. at or poleward of the cusp-

394   region). Near the winter solstices, the maximum occurrence likelihood is centred near 23–24 MLT and may be related to

395   substorm activity in this sector. The corresponding panels of Figure 7 show that the associated direction is predominantly

396   southward for NH stations (indicative of substorm-related westward currents), although curiously this is not the case for SH

397 stations. In the summer months, there is a strong clustering of events in the few hours about 11–12 MLT, which may be
398 attributed to R0 currents and ULF waves and transients in this region. Previous studies have shown that the magnitude of
399 the R0 current has a strong seasonal variation, peaking at the summer solstice (Wang et al. 2008; Milan et al. 2017). Under
400 conditions of northward IMF at the summer solstice near noon, the large dipole tilt creates an 'overdraped' magnetospheric
401 tail lobe with a magnetic field topology favourable to field-line merging with the IMF (Crooker 1992; Watanabe et al. 2005).
402 Such reconnections may drive strong impulsive field-aligned currents into the region that is poleward of the dayside cusp
403 and may explain the prevalence of extreme $|dB_H/dt|$ under these conditions.

4   Discussion

4.1   Predictions of extreme $|dB_H/dt|$

406 The Thomson et al. (2011) study of 1-minute $|dB_H/dt|$ on European magnetometers (40–74°N) predicted that, for a few
407 stations at $55 - 59$°N geomagnetic (*dipole*) latitude, 100-year return levels would increase to approximately 4000 nT/min,
408 with 200-year return levels increasing to 6000 nT/min. The highest return levels were predicted for sites BFE and ESK, which
409 are more closely separated in *CGM* latitude than in dipole latitude, laying between 52°N and 53°N CGM. This was broadly
410 supported by the Wintoft et al. (2016) analysis of 14 European stations (48–67°N geomagnetic). The return levels (RL) of the
411 present study (Figure 4), 100-year (200-year) RL (MLE) up to 2885 nT/min (4553 nT/min) at site BFE (λ = 52.0°N), are broadly
412 consistent with these earlier studies, but extend to a full range of latitudes over both hemispheres and more clearly
413 distinguish a sharp skewed peak at $|\lambda|$ = 53° in both hemispheres. The Love et al. (2016) study of 34 magnetometers
414 worldwide also predicted a sharply peaked distribution of 100-year $d|B_H|/dt$ RLs, maximising at a higher geomagnetic
415 latitude of 60° between 1000 and 2000 nT/min (see their Figure 4d), whilst the Pulkkinen et al. (2012) study of data from
416 two intense geomagnetic storms (March 1989 and Oct 2003) postulated that there is a sharp "latitude threshold" around
417 50–55° geomagnetic latitude, below which the magnitude of $|dB_H/dt|$ dropped by an order of magnitude, which is also
418 observed in Figure 4. A subsequent analysis of twelve large geomagnetic storms by Ngwira et al. (2013) confirmed that this
419 latitude threshold was associated with the limited equatorward expansion of the Auroral Electrojet (AEJ). The most extreme
420 ionospheric currents are likely to be associated with substorm expansions along auroral arcs near the edge of the auroral
421 bulge and this interpretation was recently supported by Kozyreva et al. (2018) who examined a number of substorms
422 associated with the March 2015 geomagnetic storm, observing that the maximum 1-minute fluctuations occurred near the
423 edges of the auroral electrojets, the location for which were inferred from the magnitude of the change in B_N. The bulk
424 movement of ionospheric current systems may weaken assumptions of stationarity in the tail distributions of $|dB_H/dt|$. This
425 may be of particular importance at CGM latitudes just below 53° which may be affected by extreme equatorward
426 displacements of AEJ currents under intense, and as yet unobserved, geomagnetic storm conditions. Such changes in the
427 physical environment could be addressed in future studies through physical modelling.

428 The MLT distributions of occurrence reported in this study confirm the earlier findings of Viljanen et al. (2001), who presented
429 occurrence distributions of $|dB_H/dt|$ > 1 nT/s at a number of northern European stations as a function of MLT. Similar MLT
430 and latitude distributions have been observed for Canadian magnetometers (see Fig. 3 of Boteler et al. 1998), and Beamish
431 et al. (2002) noted a local time distribution for UK magnetometers (λ = 53–62°N) with greater B_H variance in the hours
432 around local midnight, reflecting the increased substorm activity in this local time sector.

433 Viljanen et al. (2001) observed distinct peaks in the occurrence distributions around local midnight (attributed to the
434 expansion phase of substorms near the Harang discontinuity) and for auroral or higher latitude stations also in the morning
435 sector (attributed to Pc5 pulsations and omega bands), with peaks occurring around 6 MLT at auroral latitudes, or later
436 > 10 MLT at the higher-latitude Svalbard location. They also noted the strong southward direction, D, of field fluctuations
437 dB_H for large events in the auroral zone midnight sector, compared to a more East–West alignment in the morning sector.
438 Figure 7b confirms this general pattern and provides further detail as to the MLT distribution of these changes.

439 In this paper, we chose to fit the extreme $|dB_H/dt|$ data by a Generalised Pareto distribution. This generalises three classes
440 of distribution, Gumbel, Fréchet, and Weibull, which are specific cases of GP distribution with shape parameter $\xi = 0$, $\xi >$
441 0, and $\xi < 0$, respectively (Coles, 2001). The fitting is more flexible if it is not constrained to using a particular class of
442 extreme value distribution, since

443   i.   Whilst this data set hints at one class of distribution being most appropriate, this is not to say that any separate
444   but similar data set analysed in a subsequent study would give the same result. Comparison of, say, a Fréchet fit
445   to this data with a Gumbel fit to the second data set would then be harder.
446   ii.   Selecting a particular class of distribution effectively fixes the shape parameter *a priori*; thus standard error and
447   CI estimates on all return level, return period and quantile estimates would not take into account the uncertainty
448   in this choice. Retaining the more flexible GP model, in which the shape is explicitly estimated, does.

449   Wintoft et al. (2016) observed a decreasing GP distribution shape parameter, ξ, up to the highest magnetic latitude site that
450   they studied (Tromsø (λ = 67.0°N)) – with values tending towards zero or slightly negative (ξ = -0.26) at Tromsø. However,
451   our Figure 3c extends to even higher latitudes and indicates a clear local minimum in ξ at 70° with increasing shape
452   parameter, ξ at higher latitudes towards the pole, which was not previously observed. This is largely responsible for the
453   increase in predicted RLs toward the pole for return periods of 100 years or more (Figure 4). There was some evidence for
454   this trend in the 'hourly range' geomagnetic activity predictions presented by Nikitina et al. (2016) from Canadian (54°N –
455   87°N) magnetometer records, though it was not clearly evident in the study of Love et al. (2016), which fitted fixed-shape
456   (log-normal) tail distributions. If the data were log-normally distributed in the tail region, then a fit to the GP distribution
457   would yield a shape parameter ξ=0, but the analyses of Wintoft et al. (2016), Thomson et al. (2011), Weigel and Baker (2003)
458   and our own findings indicate that a heavier-tailed Fréchet distribution ($\xi > 0$) provides a better model fit, except perhaps
459   for a small number of stations at auroral latitudes.

460
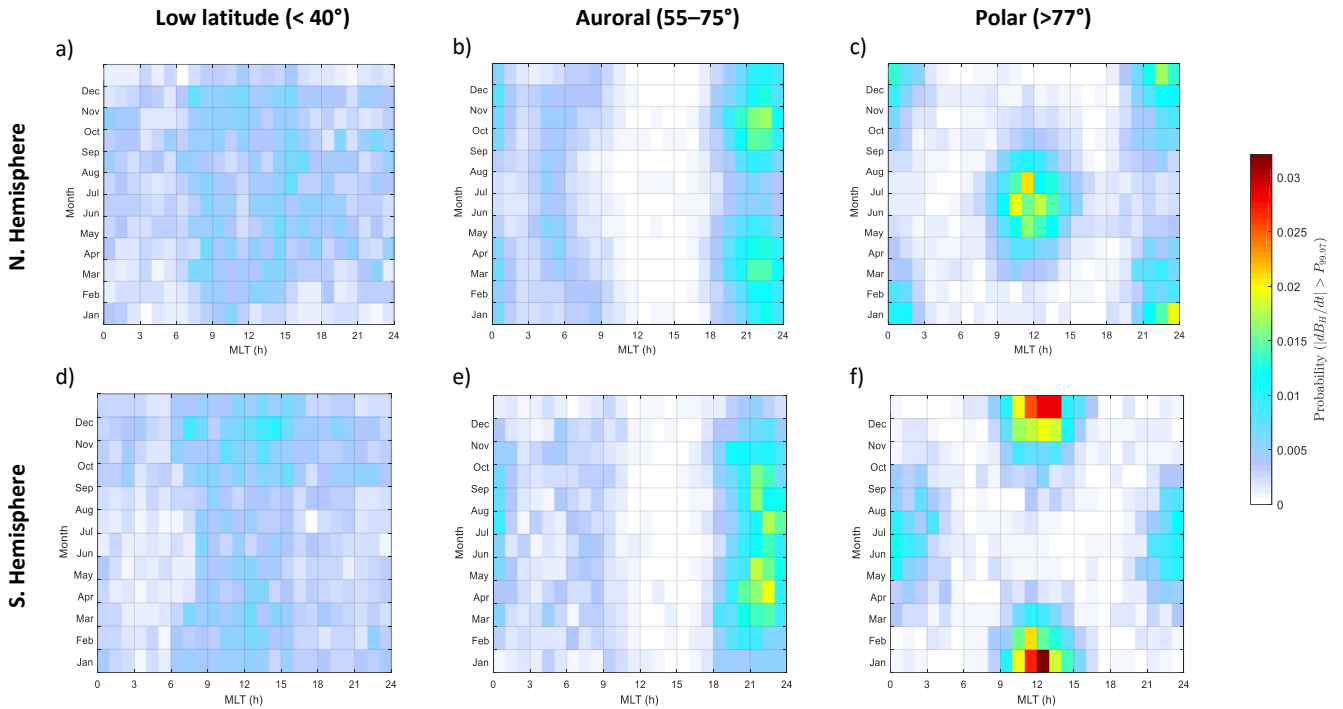
Figure 6. Occurrence probability of $|dB_H/dt| > P_{99.97}$ (after declustering) as a function of month and MLT. Panels (a) –(c) are for NH stations, whilst (d)–(f) represent SH stations. (a) and (d) represent low-latitude stations (<40° CGM), (b) and (e) represent auroral latitudes 55–75° CGM) and (c) and (f) represent latitudes above 77° CGM.
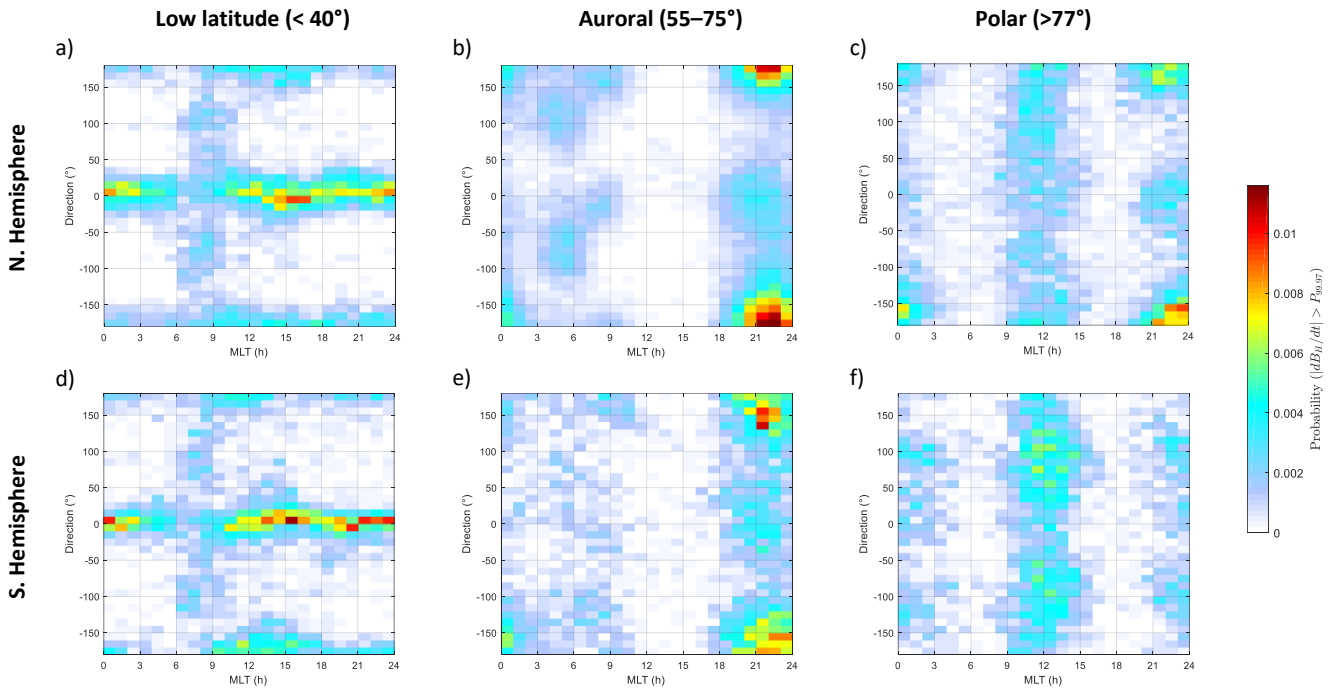
Figure 7. Occurrence probabilities in the same format as Figure 6 but shown as a function of dB_H direction, *D*, and MLT. Bin sizes are 1 hour $\times$ 10°.

4.2 Relation to Sudden Commencement timings

To illustrate the importance of SC in relation to extreme $|dB_H/dt|$ events, Figure 8 presents the likelihood that cluster peaks of $|dB_H/dt| > P_{99.97}$ occurred within a) 5 minutes, b) 5 hours, and c) 5 days of a preceding sudden commencement. The SC times were obtained from IAGA bulletins (Ebre Observatory, available online: http://www.obsebre.es/en/rapid) and filtered to retain only those events for which a majority of the five reporting magnetometers attributed a confidence factor of 2 or more (i.e. "unmistakeably a Sudden Commencement").

472 For CGM latitudes below 55°, SC occurrences within 5 minutes account for up to 50% of the cluster peaks, with a greater
473 proportion on the night side. The proportion of events preceded by SC reduces in regions of high occurrence probability (*cf*.
474 Figure 5b) and only a small proportion (< 5%) of the cluster peaks at latitudes and MLT sectors associated with auroral
475 substorms onsets, the dayside cusp, and Pc5 wave activity, are immediately preceded by SC. However, the extreme
476 $|dB_H/dt|$ events occurring at CGM latitudes above 80° in the few hours around 6 and 18 MLT are highly likely to have been
477 immediately preceded by a SC (with 30–50% of these events occurring within 5 minutes).

478 It is interesting to observe differences between the pre- and post-midnight distributions at 20° $<|\lambda|$ < 55° (Figure 8a and b),
479 where the post-midnight distribution has a greater probability of association with SC and is sharply bounded at approximately
480 6 MLT. For the dayside (6-18 MLT) region at 47° $<|\lambda|$ < 67°, the strong association with SC is observed within 5 days (Figure
481 8c) but not within 5 hours of the SC (Figure 8b), suggesting a possible connection to the later phases of geomagnetic storms.
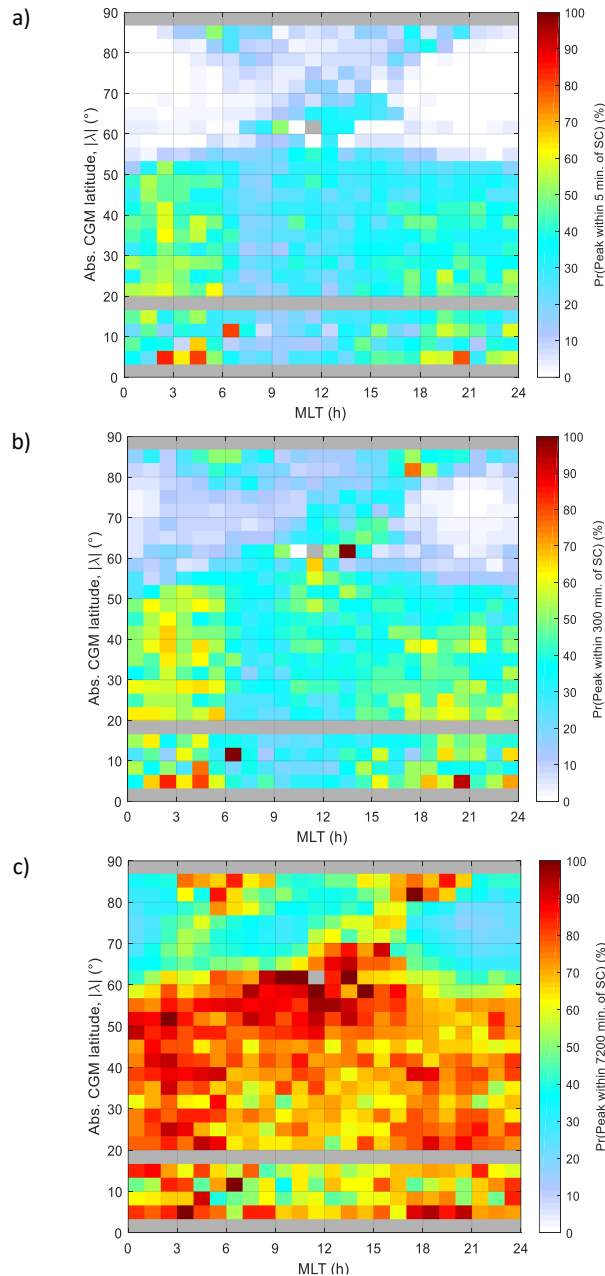
Figure 8. Fraction of cluster peaks occurring within a) 5 minutes, b) 5 hours and c) 5 days of a preceding SC.

483   ## 4.3   Dependence on IMF orientation

484   A clearer understanding of the magnetospheric drivers of very large $|dB_H/dt|$ is gained by examining the distribution of
485   cluster peaks ($|dB_H/dt| > P_{99.97}$) after filtering for the IMF field orientation. Figure 9 presents the cluster peak occurrence
486   probability distribution as shown in Figure 5b but after the dataset has been partitioned into conditions of a) northward IMF
487   ($B_z > 2$nT), b) low $|B_z| < 2$ nT, and c) southward IMF ($B_z < $ -2nT). At low- to mid-latitudes ($|\lambda| < 50°$) the occurrence
488   distributions are relatively independent of B_z, as indeed the Chapman-Ferraro currents associated with sudden
489   commencements are little influenced by the IMF B_z orientation. In the auroral region ($55° < |\lambda| < 75°$), however, the
490   peaks in the 20–24 MLT sector dominate during negative B_z – the condition necessary for substorms driven by magnetic field
491   line reconnection in the magnetotail. The occurrences at 3–6 MLT near $|\lambda| = 64°$ are also enhanced under conditions of
492   negative B_z. Positive B_z conditions lead to more frequent occurrences near the dayside cusp around noon (10–14 MLT) and
493   in the 7–10 MLT sector at $|\lambda| = 60$–80°, which are regions associated with strong Pc5 wave activity.

494
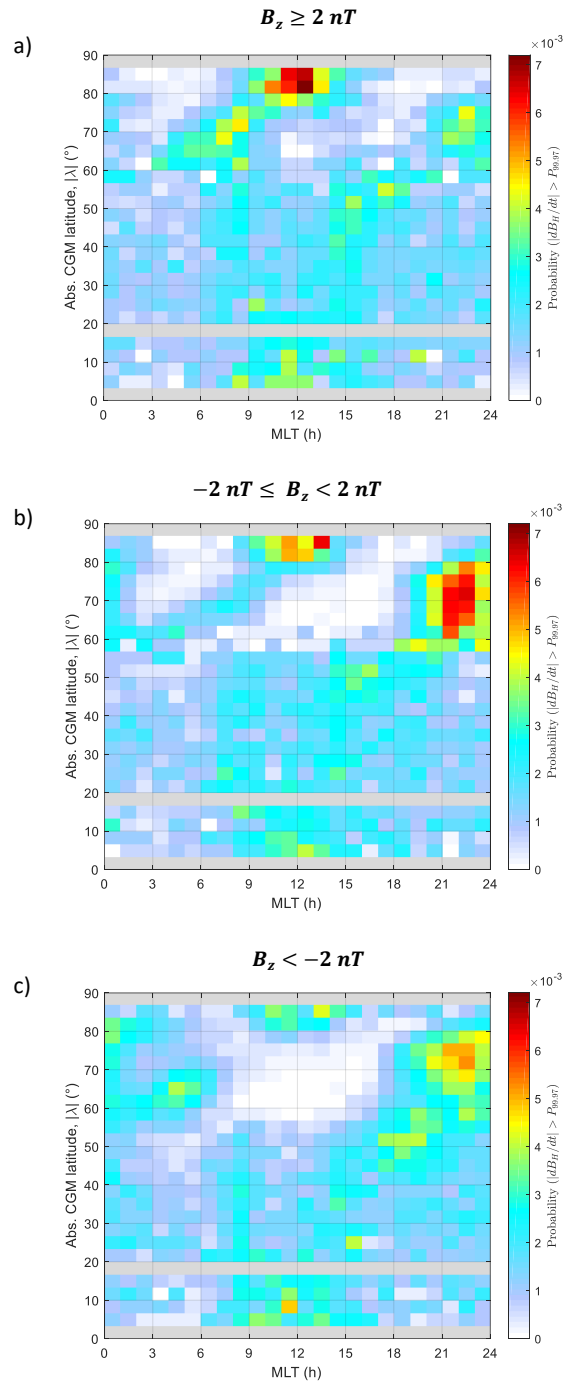
Figure 9. Probability distribution of cluster peaks as for Figure 5b) but with data filtered by IMF B_z: a) B_z > 2nT, b) -2nT <= B_z < 2nT, c) B_z < -2nT.

In Figure 10 we examine data from magnetometers in the auroral region ($|\lambda| = 55$–75 °N) and further partition the cluster peaks by both B_y and B_z. In all MLT sectors, cluster peaks for negative B_z (panels *g–i*) occur most frequently at the vernal equinox for negative B_y (panel *g*) and at the autumnal equinox for positive B_y (panel *i*). The converse is true under positive B_z conditions (panels *a–c*) with cluster peaks occurring most frequently at the autumnal (vernal) equinox under negative (positive) B_y conditions. These patterns indicate a strong relation to the Russell-McPherron effect, which ascribes seasonal and diurnal changes in magnetic field line reconnection and geomagnetic activity to changes in the orientation of the Earth's dipole axis with respect to the IMF (Russell & McPherron 1973).

Previous studies have shown that the MLT of the cusp region is controlled by the IMF B_y component. In the northern hemisphere, the cusp is shifted pre-noon (post-noon) for negative (positive) B_y, with the opposite behaviour in the southern hemisphere. This shift is more pronounced under negative B_z conditions when the cusp lies further equatorward (Newell et

507   al. 1989). To examine the effect this might have on the distribution of cluster peaks ($|dB_H/dt| > P_{99.97}$) an analysis of B_y

508   and B_z dependences is presented in Figure 11 for all magnetometers in the NH cusp and polar region, $|\lambda| > 77°$N. This shows

509   that under all conditions of B_z, the locus of cluster peaks ($|dB_H/dt| > P_{99.97}$) shifts from about 10:30 MLT for negative B_y

510   conditions, to about 12:30 MLT for positive B_y.

511   The polarity of the R0 field-aligned currents entering the cusp region have been previously shown to depend on the IMF B_y

512   component, (being upward (downward) in the northern hemisphere (NH) for $B_y > 0$ ($B_y < 0$), and opposite in the southern

513   hemisphere (SH)) (Milan et al. 2017, and references therein). However, we found that the direction, D, of the peak

514   fluctuations for $|\lambda| > 77°$N near local noon (not shown) was relatively uniform (isotropic) and did not change significantly

515   with B_y or B_z. This indicates that the magnetic fluctuations associated with field-aligned currents are too weak to

516   significantly affect the highest percentiles of $|dB_H/dt|$, due in part to the shielding effect of the conductive ionospheric layer.
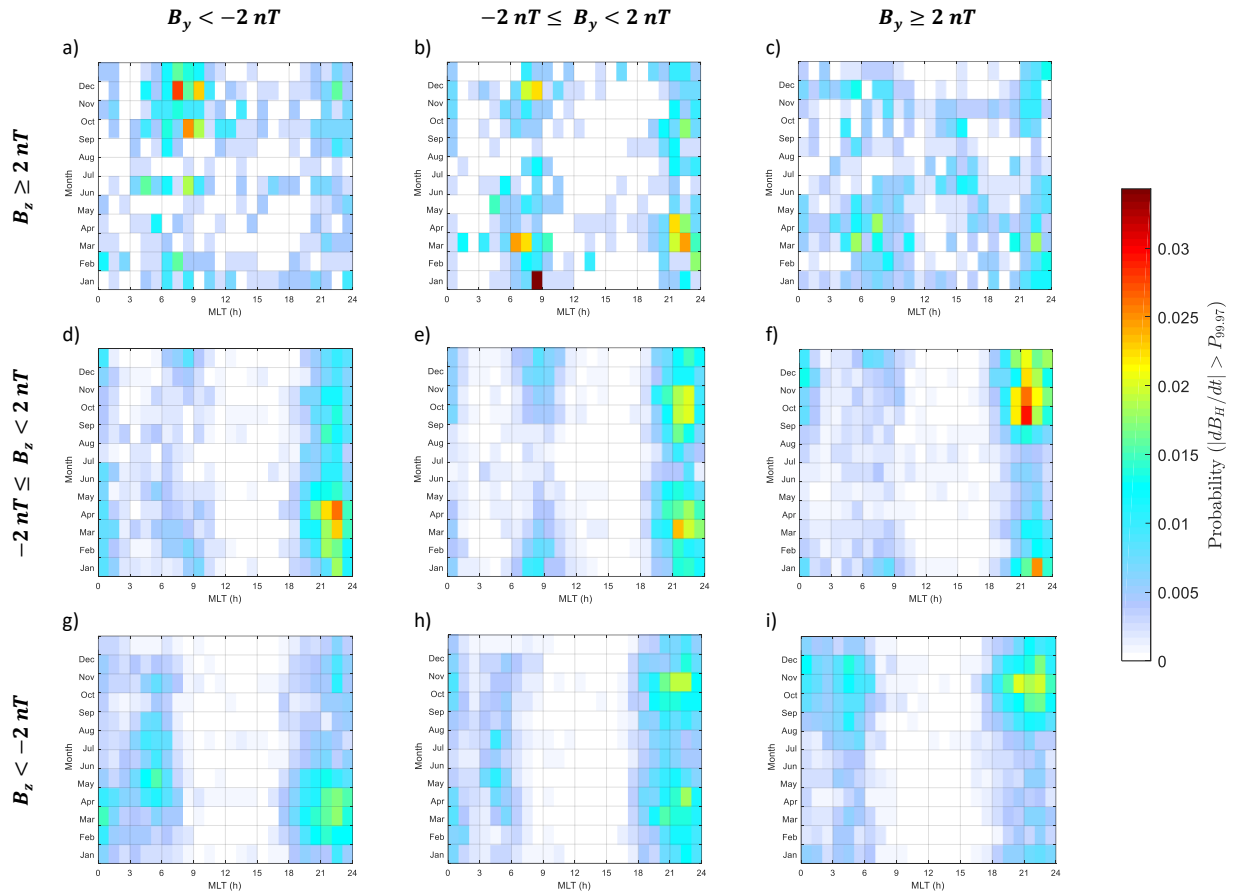
Figure 10. Occurrence probability of $|dB_H/dt| > P_{99.97}$ (after declustering) as a function of month and MLT, for NH stations between 55°N and 75°N CGM, filtered by IMF orientation: Panels a–c) $B_z \geq 2$ nT, d–f) -2 nT $\leq Bz <$ 2 nT, g–i) $B_z \geq$ 2nT, Panels a,d,g) $B_y <$-2 nT; panels b,e,h) -2 nT $\leq B_y <$ 2 nT; panels c,f,i) $B_y \geq 2$ nT.
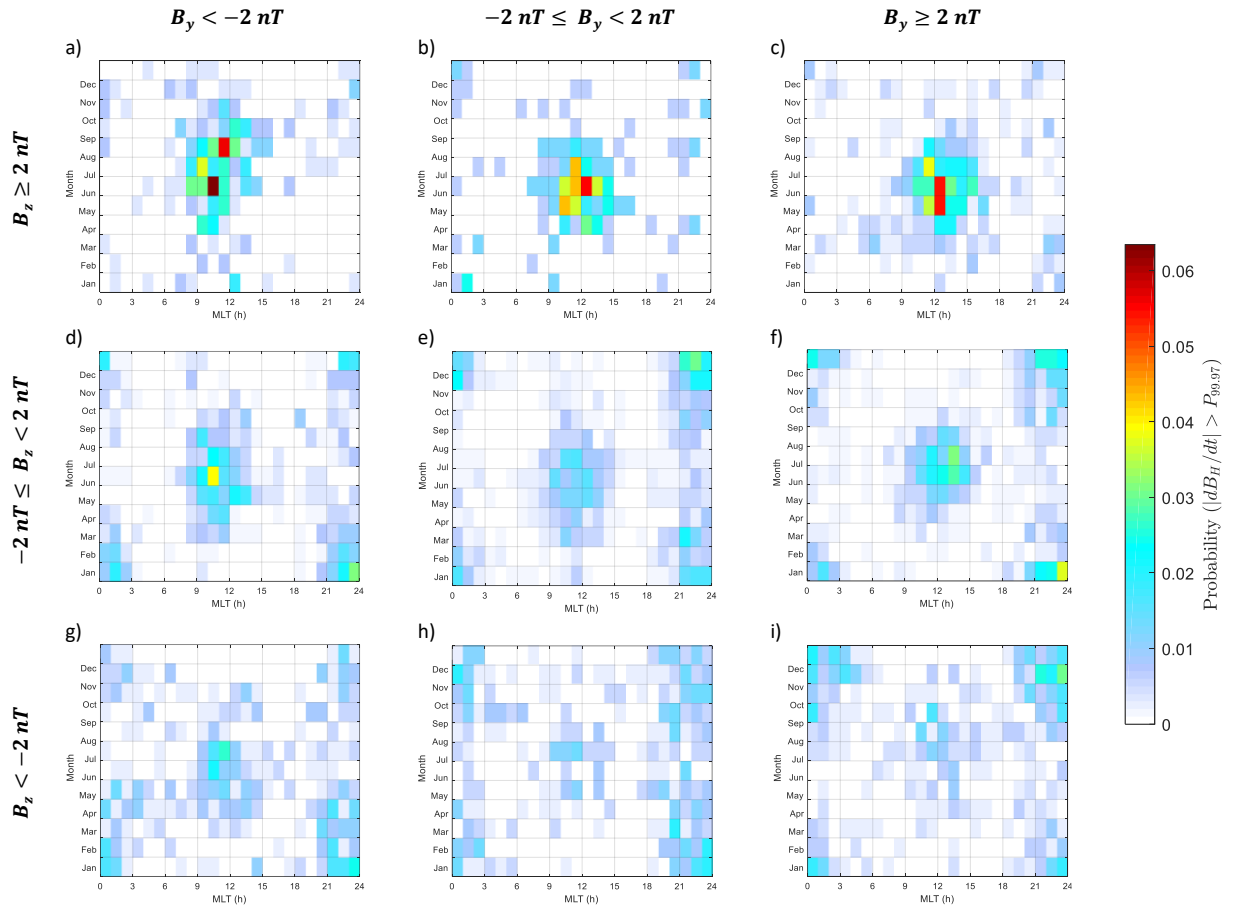
Figure 11. As Figure 10, but for NH stations above 77°N CGM.

5   Summary and Conclusions

In this study we have used Extreme Value Theory (EVT) to fit Generalised Pareto (GP) tail distributions to a large global data set of horizontal magnetic field fluctuations, dB_H/dt from 125 magnetometers. The variation of the fitted GP parameters and derived 5- to 500-year return levels (RL) have been modelled as functions of the corrected geomagnetic (CGM) latitude, λ. A combination of high scale (σ) and shape (ξ) parameters in the region of $|\lambda|$=53° (in both hemispheres) creates a sharp maximum in RL at this latitude. Values of ξ increasing above $|\lambda|$=75° lead to a trend towards increasing RLs for locations in the polar cap for return periods greater than 100 years.

The rate of occurrence of $|dB_H/dt|$ measurements exceeding the 99.97th percentile ($P_{99.97}$) has also been modelled as a function of CGM latitude, month, MLT, and the direction of dB_H. The occurrence of large $|dB_H/dt|$ has been shown to be strongly dependent on CGM latitude and MLT sector, such that a GIC observed in one ground-based system can be expected to differ greatly from that in others well-separated in latitude or longitude (or local time). By fitting analytical surfaces (such as a polynomial or spherical harmonic expansion) to the 2-d occurrence probability profile, e.g. $P(|dB_H/dt| > P_{99.97}; \lambda, MLT)$ a fully analytical model of return levels may be generated, parameterised by these covariates.

The occurrence probability profile has distinct maxima in the pre-midnight auroral zone ($|\lambda|$ = 55–75°), with predominantly southward dB_H, that may be attributed to substorm-related westward ionospheric currents.   The probability maximises near the equinoxes (with a secondary winter maximum) principally under conditions of negative IMF B_z.

The auroral zone 03–11 MLT sector is characterised by an increase in event occurrences that matches known patterns of ULF Pc5 wave activity. Events occur preferentially at earlier local times and at lower latitudes under negative B_z, with a more isotropic directional distribution centred broadly about the 100° – 280° bearing axis.   In the northern hemisphere (at least), the earlier MLT occurrences are principally observed near the June solstice, with later MLT occurrences towards December.

541 Both substorm-related and Pc5-related peaks (at all local times) exhibit a seasonal dependence on IMF orientation consistent
542 with the Russell-McPherron effect.

543 In the region poleward of the polar cusp $|\lambda|>75°$ in the summer months there is a raised probability of occurrence at 10–14
544 MLT, peaking slightly earlier (later) for negative (positive) IMF B_y, with greater occurrence probability under positive B_z
545 conditions. The directional distribution of these changes is nearly isotropic.

546 At low latitudes ($|\lambda|<40°$), occurrence probability $P(|dB_H/dt| > P_{99.97}; \lambda, MLT)$ forms a V-shaped distribution in latitude
547 versus MLT, closely distributed about 11 MLT at the equator but extended towards dawn and dusk towards mid-latitudes.
548 Large magnetic field fluctuations in this region are principally northward directed, and may be attributed to sudden
549 commencements (SC). There is a raised probability of events being observed within 5-minutes of a SC in latitude zones and
550 MLT sectors for which there are relatively few occurrences (night-side, low latitude, or near dawn or dusk at polar-latitudes
551 ($|\lambda|>80°$).

552 Results from this study may be applied in the evaluation and mitigation of GIC risks. Models of maximum likelihood estimates
553 for $|dB_H/dt|$ *vs* geomagnetic latitude (Section 3.1) are provided for return periods of up to 500 years. Combining these
554 predictions with an Earth conductivity model would yield predictions of the extreme geoelectric fields induced at the Earth's
555 surface. When these are input to engineering models, such as HV electricity network models, the return levels for GICs may
556 be estimated. Models of the occurrence probability of $P(|dB_H/dt| > P_{99.97})$ with month and MLT may be used to refine RL
557 estimates of $|dB_H/dt|$ for operations limited to certain seasons or times of day. Furthermore, information from the pattern
558 of occurrence probability *vs* direction (Figure 7) could be used to refine GIC risk estimates for individual linear components
559 of ground infrastructure, such as sections of pipeline, cables, or elements of an HV electricity network.

560 It should be noted that the statistics presented in this paper reflect only the minute-to-minute changes in magnetic field.
561 Further studies (not reported here) have examined the directional statistics of magnetic field fluctuations on longer time
562 scales up to 60 minutes, which are also important for GIC modelling but are governed by different temporal characteristics
563 of the ionospheric and magnetospheric current systems. We shall report these findings in a future paper. Sub-minute
564 geomagnetic field fluctuations are also effective in inducing surface electric fields from shallow depths in the Earth and these
565 will be examined in future studies using a much more limited set of magnetograms recorded at 1- or 10-s cadence.

566

References

587 Baker, KB, and Wing, S. 1989. A new magnetic coordinate system for conjugate studies at high latitudes, *J. Geophys. Res.* **94**: 9139–9143.
588 DOI: 10.1029/JA094iA07p09139.

Baker, G, Donovan, EF, and Jackel, BJ. 2003. A comprehensive survey of auroral latitude Pc5 pulsation characteristics, *J. Geophys. Res.* **108**: 1384. DOI: 10.1029/2002JA009801.

Beamish, D, Clark, TDG, Clarke, E, and Thomson, AWP. 2002. Geomagnetically induced currents in the UK: geomagnetic variations and surface electric fields, *J. Atmos. Solar-Terr. Phys.* **64**: 1779–1792. DOI: 10.1016/S1364-6826(02)00127-X.

Beggan, CD, Beamish, D, Richards, A, Kelly, GS, and Thomson, AWP. 2013. Prediction of extreme geomagnetically induced currents in the UK high-voltage network. *Space Weather* **11**: 407–419. DOI: 10.1002/swe.20065.

Belakhovsky, VB, Pilipenko, VA, Sakharov, YaA, Lorentzen, DL, and Samsonov, SN. 2017. Geomagnetic and ionospheric response to the interplanetary shock on January 24, 2012. *Earth Planets Space* **69**: 105. DOI: 10.1186/s40623-017-0696-1.

Belakhovsky V, Pilipenko, V, Engebretson, M, Sakharov, Y, and Selivanov, V. 2019. Impulsive disturbances of the geomagnetic field as a cause of induced currents of electric power lines *J. Space Weather Space Clim.* **9**: A1. DOI: 10.1051/swsc/2019015.

Boteler, DH. 2000. Geomagnetic effects on the pipe-to-soil potentials of a continental pipeline, *Adv. Space Res.* **26:** 15—20. DOI: 10.1016/S0273-1177(99)01020-0.

Boteler, DH, and Pirjola, RJ. 2014. Comparison of methods for modelling geomagnetically induced currents, *Ann. Geophys.* **32**: 1177–1187, DOI: 10.5194/angeo-32-1177-2014.

Boteler, DH, and Pirjola, RJ. 2017. Modeling geomagnetically induced currents. *Space Weather* **15**: 258–276. DOI: 10.1002/2016SW001499.

Boteler, DH, Pirjola, RJ, and Nevanlinna H. 1998. The effects of geomagnetic disturbances on electrical systems at the Earth's surface, *Adv Space Res.* **22**: 17–27. DOI: 10.1016/S0273-1177(97)01096-X.

Cagniard, L. 1953. Basic theory of the magneto-telluric method of geophysical prospecting. *Geophysics* **18**: 605–635. DOI: 10.1190/1.1437915.

Campbell, WH. 2003. Introduction to geomagnetic fields. 2nd Ed., Cambridge University Press, Cambridge, UK. ISBN: 0521529530.

Carter, BA, Yizengaw, E, Pradipta R, Halford AJ, Norman R, and Zhang, K. 2015. Interplanetary shocks and the resulting geomagnetically induced currents at the equator. *Geophys. Res. Lett.* **42**: 6554–6559. DOI: 10.1002/2015GL065060.

Chapman, S, and Ferraro, VCA . 1931. A new theory of magnetic storms. *Terr. Magn.* **36**: 77–97. DOI: 10.1029/TE036i002p00077.

Coles, S. 2001. An introduction to statistical modeling of extreme values. *Springer-Verlag, London ltd.*. DOI: 10.1007/978-1-4471-3675-0.

Crooker, NU. 1992. Reverse convection, *J. Geophys. Res.* **97**: 19363–19372. DOI: 10.1029/92JA01532.

Elvidge, S, and Angling, M. 2018. Using extreme value theory for determining the probability of Carrington-like solar flares. *Space Weather* **16**: 417—421. DOI: 10.1002/2017SW001727.

Engebretson, M, Glassmeier, K-H, Stellmacher, M, Hughes WJ, and Lühr, H. 1998. The dependence of high-latitude Pc5 wave power on solar wind velocity and on the phase of high-speed solar wind streams, *J. Geophys. Res.* **103**: 26271–26283. DOI: 10.1029/97JA03143.

Engebretson, MJ, Yeoman, TK, Oksavik, K, Søraas, F, Sigernes, F, et al.. 2013. Multi-instrument observations from Svalbard of a traveling convection vortex, electromagnetic ion cyclotron wave burst, and proton precipitation associated with a bow shock instability. *J. Geophys. Res.* **118**: 2975–2997. DOI: 10.1002/jgra.50291.

Erinmez, IA, Kappenman, JG, and Radasky, WA. 2002. Management of the geomagnetically induced current risks on the National Grid company's electric power transmission system, *J. Atmos. Solar-Terr. Phys.* **64**: 743–756. DOI: 10.1016/S1364-6826(02)00036-6.

Eroshenko, EA, Belov, AV, Boteler, DH, Gaidash, SP, Lobkov, SL, Pirjola, and Trichtchenko, L. 2010. Effects of strong geomagnetic storms on northern railways in Russia. *Adv. Space Res.* **46**: 1102–1110. DOI: 10.1016/j.asr.2010.05.017.

Falayi, EO, Ogunmodimu, O, Bolaji, OS, Ayanda, JD, and Ojoniyi, OS. 2017. Investigation of geomagnetic induced current at high latitude during the storm-time variation. *NRIAG Journal of Astronomy and Geophysics* **6**: 131–140. DOI: 10.1016/j.nrjag.2017.04.010.

Fiori, RAD, Boteler, DH, and Gillies, DM. 2014. Assessment of GIC risk due to geomagnetic sudden commencements and identification of the current systems responsible. *Space Weather* **12**: 76–91. DOI: 10.1002/2013SW000967.

Friis-Christensen, E, McHenry, MA, Clauer, CR, and Vennerstrøm, S. 1988. Ionospheric traveling convection vortices observed near the polar cleft: A triggered response to sudden changes in the solar wind. *Geophys Res Lett.* **15**: 253–256. DOI: 10.1029/GL015i003p00253.

Gaunt, CT, and Coetzee G. 2007. Transformer failures in regions incorrectly considered to have low GIC-risk. *IEEE PowerTech, Lausanne, 1–5 July 2007*, 807–812. DOI: 10.1109/PCT.2007.4538419.

Gjerloev, JW. 2009. A global ground-based magnetometer initiative, *Eos* **90**: 230–231. DOI: 10.1029/2009EO270002.

Gjerloev, JW. 2012. The SuperMAG data processing technique, *J. Geophys. Res.* **117**: A09213. DOI: 10.1029/2012JA017683.

Gjerloev, JW, Hoffman, RA, Sigwarth, JB, and Frank, LA. 2007. Statistical description of the bulge-type auroral substorm in the far ultraviolet. *J. Geophys. Res.* **112**: A07213. DOI: 10.1029/2006JA012189.

Gjerloev, JW, and Hoffman RA. 2014. The large-scale current system during auroral substorms. *J. Geophys. Res. Space Physics* **119**, 4591–4606. DOI: 10.1002/2013JA019176.

Hao, YX, Zong, Q-G, Zhou, X-Z, Rankin, R, Chen, XR, Liu, Y, et al.. 2019. Global-scale ULF waves associated with SSC accelerate magnetospheric ultrarelativistic electrons. *J. Geophys Res*. *Space Physics* **124**: 1525–1538. DOI: 10.1029/2018JA026134.

Hunsucker, RD, and Hargreaves, JK. 2003. The high-latitude ionosphere and its effects on radio propagation. *Cambridge University Press.* ISBN 0 521 33083 1.

Kappenman, JG. 2003. Storm sudden commencement events and the associated geomagnetically induced current risks to ground-based systems at low-latitude and midlatitude locations. *Space Weather* **1**: 1016. DOI: 10.1029/2003SW000009.

Kappenman, JG. 2004. The evolving vulnerability of electric power grids. *Space Weather* **2**: S01004. DOI: 10.1029/2003SW000028.

Kappenman, JG. 2006. Great geomagnetic storms and extreme impulsive geomagnetic field disturbance events – An analysis of observational evidence including the great storm of May 1921. *Adv. Space Res.* **38**: 188–199. DOI: j.asr.2005.08.055.

Kivelson, MG, and Russell CT. 2005. Introduction to space physics. *Cambridge University Press*. ISBN: 9780521457149.

Knipp, DJ. 2011. Understanding space weather and the physics behind it. *McGraw-Hill Companies, Inc.* ISBN: 9780073408903.

Koons, HC. 2001. Statistical analysis of extreme values in space science, *J. Geophys. Res.* **106**: 10,915–10,921. DOI: 10.1029/2000JA000234

651 Kozyreva, OV, Pilipenko, VA, Belakhovsky, VB, and Sakharov, YA. 2018. Ground geomagnetic field and GIC response to March 17, 2015,
652   storm. *Earth, Planets, Space* **70**: 157. DOI: 10.1186/s40623-018-0933-2.

653 Lanzerotti, LJ, Konik, RM, Wolfe, A, Venkatesan, D, and Maclennan, CG. 1991. Cusp latitude magnetic impulse events: 1.Occurrence statistics,
654   *J. Geophys. Res.* **96**: 14009–14022. DOI: 10.1029/91JA00567.

655 Lanzerotti, LJ, Medford, LV, Maclennan, CG, and Thomson, DJ. 1995. Studies of large-scale Earth potentials across oceanic distances. *AT&T*
656   *Technical Journal* **74**: 73–84. DOI: j.1538-7305.1995.tb00185.x.

657 Laundal, KM, and Richmond, AD. 2017. Magnetic coordinate systems. *Space Sci. Rev*. **206**: 27. DOI: 10.1007/s11214-016-0275-y.

658 Liou, K, Newell, PT, Sibeck, DG, and Meng, C-I. 2001. Observation of IMF and seasonal effects in the location of auroral substorm onset. *J.*
659   *Geophys. Res*. **106**: 5799–5810. DOI: 10.1029/2000JA003001

660 Liu, L, Ge, X, Zong, W, Zhou, Y, and Liu, M. 2016. Analysis of the monitoring data of geomagnetic storm interference in the electrification
661   system of a high-speed railway. *Space Weather* **14**: 754–763. DOI: 10.1002/2016SW001411.

662 Love, JL, Coïsson, P, and Pulkkinen, A. 2016. Global statistical maps of extreme-event magnetic observatory 1 min first differences in
663   horizontal intensity. *Geophys. Res. Lett*. **43**: 4126–4135. DOI : 10.1002/2016GL068664.

664 Manpreet, K. 2018. Geomagnetic Disturbance Characterization in the Hydro-Quebec power system using AUTUMNX data. *MEng. thesis*,
665   *University   of   Victoria,   Canada.*   Available   online:
666   https://dspace.library.uvic.ca/bitstream/handle/1828/9018/Kaur_Manpreet_MEng_2018.pdf.

667 Marshall, RA, Dalzell, M, Waters, CL, Goldthorpe, P, and Smith, EA. 2012. Geomagnetically induced currents in the New Zealand power
668   network. *Space Weather* **10**: S08003. DOI: 10.1029/2012SW000806.

669 Masson, A, and Nykyri, K. 2018. Kelvin–Helmholtz instability: Lessons learned and ways forward. *Space Sci. Rev*. **214**: 71, 10.1007/s11214-
670   018-0505-6.

671 Matsushita, S. 1968. Sq and L current systems in the ionosphere. *Geophys. J. International*, **15:** 109–125. DOI: 10.1111/j.1365-
672   246X.1968.tb05751.x.

673 Menietti, JD, and Burch, JL. 1988. Spatial extent of the plasma injection region in the cusp-magnetosheath interface. *J. Geophys. Res*. **93**:
674   105–113. DOI: 10.1029/JA093iA01p00105.

675 Meredith, NP, Horne, RB, Isles, JD, and Rodriguez, JV. 2015. Extreme relativistic electron fluxes at geosynchronous orbit: Analysis of GOES E
676   >2 MeV electrons. *Space Weather* **13**: 170–184. DOI: 10.1002/2014SW001143.

677 Milan, SE, Clausen, LBN, Coxon, JC, Carter, JA, Walach, M-T, et al. 2017. Overview of solar wind–magnetosphere–ionosphere–atmosphere
678   coupling and the generation of magnetospheric currents. *Space Sci. Rev*. **206**: 547. DOI: 10.1007/s11214-017-0333-0.

679 Molinski, TS. 2002. Why utilities respect geomagnetically induced currents. *J. Atmos. Solar-Terr. Phys*. **64**: 1765– 1778. DOI: 10.1016/S1364-
680   6826(02)00126-8.

681 Nakamura, M, Yoneda, A, Oda, M, and Tsubouchi, K. 2015. Statistical analysis of extreme auroral electrojet indices. *Earth, Planets, Space.*
682   **67**: 153. DOI: 10.1186/s40623-015-0321-0.

683 Newell, PT, Meng, C-I, Sibeck, DG and Lepping, R. 1989. Some low-altitude cusp dependencies on the interplanetary magnetic field. *J.*
684   *Geophys. Res.* **94**: 8921–8927. DOI:10.1029/JA094iA07p08921.

685 Ngwira, CM, Pulkkinen, A, Wilder, FD, and Crowley, G. 2013. Extended study of extreme geoelectric field event scenarios for geomagnetically
686   induced current applications. *Space Weather* **11**: 121–131. DOI: 10.1002/swe.20021.

687 Ngwira, CM, Sibeck, D, Silveira, MDV, Georgiou, M, Weygand, JM, Nishimura, Y, and Hampton, D. 2018. A study of intense local dB/dt
688   variations during two geomagnetic storms. *Space Weather* **16**: 676–693. DOI: 10.1029/2018SW001911.

689 Nikitina, L, Trichtchenko, L, and Boteler, DH. 2016. Assessment of extreme values in geomagnetic and geoelectric field variations for Canada.
690   *Space Weather* **14**: 481–494. DOI: 10.1002/2016SW001386.

691 Nykyri, K, and Dimmock, AP. 2016. Statistical study of the ULF Pc4–Pc5 range fluctuations in the vicinity of Earth's magnetopause and
692   correlation with the Low Latitude Boundary Layer thickness. *Adv. Space Sci*. **58**: 257–267. DOI: 10.1016/j.asr.2015.12.046.

693 O'Brien, TP, Fennell, JF, Roeder, JL, and Reeves, GD. 2007. Extreme electron fluxes in the outer zone. *Space Weather* **5**: S01001. DOI:
694   10.1029/2006SW000240.

695 Pahud, DM, Rae, IJ, Mann, IR, Murphy, KR, and Amalraj, V. 2009. Ground-based Pc5 ULF wave power: Solar wind speed and MLT dependence.
696   *J. Atmos. Terr. Phys*. **71**: 1082–1092. DOI: 10.1016/j.jastp.2008.12.004.

697 Pawitan, Y. 2001. In all likelihood: statistical modelling and inference using likelihood. *Oxford; New York: Clarendon Press*: ISBN:
698   9780191650574 (e-book).

699 Pirjola, R, Viljanen, A, Pulkkinen, A, and Amm, O. 2000. Space weather risk in power systems and pipelines. *Physics and Chemistry of the*
700   *Earth, Part C: Solar, Terr. & Planetary Science* **25**: 333–337. DOI: 10.1016/S1464-1917(00)00027-1.

701 Pirjola, R. 2002. Review on the calculation of surface electric and magnetic fields and of geomagnetically induced currents in ground-based
702   technological systems. *Surveys in Geophysics* **23**: 71–90. DOI: 10.1023/A:101481600930.

703 Pitout, F, Bosqued, J-M, Alcaydé, D, Denig, WF, and Rème, H. 2001. Observations of the cusp region under northward IMF. *Ann. Geophys*.
704   **19**: 1641–1653. DOI: 10.5194/angeo-19-1641-2001.

705 Pothier, NM, Weimer, DR, and Moore, WB. 2015. Quantitative maps of geomagnetic perturbation vectors during substorm onset and
706   recovery. *J. Geophys. Res.: Space Physics* **120**: 1197–1214. DOI: 10.1002/2014JA020602.

707 Pulkkinen, A, Viljanen, A, Pajunpää, K, and Pirjola, R. 2001. Recordings and occurrence of geomagnetically induced currents in the Finnish
708   natural gas pipeline network. *J. App. Geophys*. **48**: 219–231. DOI: 10.1016/S0926-9851(01)00108-2.

709 Pulkkinen, A, Thomson, A, Clarke, E, and McKay, A. 2003. April 2000 geomagnetic storm: ionospheric drivers of large geomagnetically
710   induced currents. *Ann. Geophys.* **21**: 709–717. DOI: 10.5194/angeo-21-709-2003.

711 Pulkkinen, A, Bernabeu, E, Eichner, J, Beggan, C, and Thomson, AWP. 2012. Generation of 100-year geomagnetically induced current
712   scenarios. *Space Weather* **10:** S04003. DOI: 10.1029/2011SW000750.

713 Qian, X, Tian, H, Yin, Y, Li, Y, Liu, M, and Jiang, Z. 2016. Geomagnetic storms' influence on intercity railway track circuit. *Urban Rail Transit*.
714   **2**: 85–91. DOI: 10.1007/s40864-016-0040-2.
715 Reiss, R-D, and Thomas, M. 2007. Statistical analysis of extreme values (3rd Ed.). *Birkhäuser Verlag, Basel-Boston-Berlin*. DOI: 10.1007/978-
716   3-7643-7399-3.
717 Root, HG. 1979. Earth-current effects on communication-cable power subsystems. *IEEE Transactions on Electromagnetic Compatibility* **EMC-**
718   **21**: 87–92. DOI: 10.1109/TEMC.1979.303750.
719 Russell, CT, and Elphic, RC. 1978. Initial ISEE magnetometer results: magnetopause observations. *Space Sci. Rev.* **22**: 681. DOI:
720   10.1007/BF00212619 .
721 Russell, CT, and McPherron, RL. 1973. Semiannual variation of geomagnetic activity. *J. Geophys. Res*., **78**: 92–108. DOI:
722   10.1029/JA078i001p00092.
723 Russell, CT, Ginskey, M, and Petrinec, SM. 1994. Sudden impulses at low-latitude stations: Steady state response for northward
724   interplanetary magnetic field. *J. Geophys. Res.* **99**: 253–261. DOI: 10.1029/93JA02288.
725 Shepherd, SG. 2014. Altitude-adjusted corrected geomagnetic coordinates: definition and functional approximations. *J. Geophys. Res.* **119**:
726   7501–7521. DOI: 10.1002/2014JA020264.
727 Shinbori, A, Tsuji, Y, Kikuchi, T, Araki, T, and Watari S. 2009. Magnetic latitude and local time dependence of the amplitude of geomagnetic
728   sudden commencements. *J. Geophys. Res.* **114**: A04217. DOI: 10.1029/2008JA013871.
729 Sibeck, DG. 1993. Transient magnetic field signatures at high latitudes. *J. Geophys. Res.* **98**: 243–256. DOI: 10.1029/92JA01661.
730 Sibeck, DG, and Korotova, GI. 1996. Occurrence patterns for transient magnetic field signatures at high latitudes. *J. Geophys. Res.* **101:**
731   13413–13428. DOI: 10.1029/96JA00187.
732 Silbergleit, V. 1996. On the occurrence of geomagnetic storms with sudden commencements. *J. Geomag. Geoelectr.* **48**: 1011–1016. DOI:
733   10.5636/jgg.48.1011.
734 Silbergleit, V. 1999. Forecast of the most geomagnetically disturbed days. *Earth, Planets, Space* **51**: 19–22. DOI: 10.1186/BF03352205.
735 Siscoe, GL. 1976. On the statistics of the largest geomagnetic storms per solar cycle. *J. Geophys. Res.* **81**: 4782–4784. DOI:
736   10.1029/JA081i025p04782.
737 Thébault, E, Finlay, CC, Beggan, CD, Alken, P, Aubert, J, et al. 2015. International Geomagnetic Reference Field: the 12th generation. *Earth,*
738   *Planets, Space* **67**: 79. DOI: 10.1186/s40623-015-0228-9.
739 Thomson, AWP, Gaunt, CT, Cilliers, P, Wild, JA, Opperman, B, McKinnell L-A, Kotze, P, Ngwira, CM, and Lotz, SI. 2010. Present day challenges
740   in understanding the geomagnetic hazard to national power grids. *Adv. Space Res.* **45:** 1182-1190. DOI: 10.1016/j.asr.2009.11.023.
741 Thomson, AWP, Dawson, EB, and Reay, SJ. 2011. Quantifying extreme behavior in geomagnetic activity. *Space Weather* **9**: S10001. DOI:
742   10.1029/2011SW000696.
743 Trivedi, NB, Vitorello, Í, Kabata, W, Dutra, SLG, Padilha, AL, et al. 2007. Geomagnetically induced currents in an electric power transmission
744   system at low latitudes in Brazil: A case study. *Space Weather* **5**: S04004. DOI: 10.1029/2006SW000282.
745 Tsiftsi, T, and De la Luz, V. 2018. Extreme value analysis of solar flare events. *Space Weather* **16**: 1984–1986. DOI: 10.1029/2018SW001958.
746 Tsubouchi, K, and Omura, Y. 2007. Long-term occurrence probabilities of intense geomagnetic storm events. *Space Weather* **5**: S12003. DOI:
747   10.1029/2007SW000329.
748 Vasseur, G, and Weidelt, P. 1977. Bimodal electromagnetic induction in non-uniform thin sheets with an application to the northern
749   Pyrenean induction anomaly. *Geophysical Journal International* **51**: 669–690. DOI: 10.1111/j.1365-246X.1977.tb04213.x.
750 Vennerstrøm, S. 1999. Dayside magnetic ULF power at high latitudes: A possible long-term proxy for the solar wind velocity? *J. Geophys.*
751   *Res.* **104:** 10145–10157. DOI: 10.1029/1999JA900015.
752 Viljanen, A, Nevanlinna, H, Pajunpää, K, and Pulkkinen, A. 2001. Time derivative of the horizontal geomagnetic field as an activity indicator.
753   *Ann. Geophys.* **19**: 1107–1118. DOI: 10.5194/angeo-19-1107-2001.
754 Vorobjev, VG, Yagodkina, OI, and Zverev, VL. 1999. Morphological features of bipolar magnetic impulsive events and associated
755   interplanetary medium signatures. *J. Geophys. Res.* **104**: 4595– 4607. DOI: 10.1029/1998JA900042.
756 Wang, H, Lühr, H, Ma, SY, and Ritter, P. 2005. Statistical study of the substorm onset: its dependence on solar wind parameters and solar
757   illumination. *Ann. Geophys.* **23**: 2069–2079. DOI: 10.5194/angeo-23-2069-2005.
758 Wang, H, Ridley, AJ, and Lühr, H. 2008. SWMF simulation of field-aligned currents for a varying northward and duskward IMF with nonzero
759   dipole tilt, *Ann. Geophys.* **26**: 1461–1477. DOI: 10.5194/angeo-26-1461-2008.
760 Watanabe, M, Kabin, K, Sofko, GJ, Rankin, R, Gombosi, TI, Ridley, AJ, and Clauer, CR. 2005. Internal reconnection for northward
761   interplanetary magnetic field, *J. Geophys. Res.* **110**: A06210. DOI: 10.1029/2004JA010832.
762 Weigel, RS, and Baker, DN. 2003. Probability distribution invariance of 1-minute auroral-zone geomagnetic field fluctuations. *Geophys. Res.*
763   *Lett.* **30**: 2193. DOI: 10.1029/2003GL018470.
764 Weimer, DR, Ober, DM, Maynard, NC, Collier, MR, McComas, DJ, Ness, NF, Smith, SW, and Watermann, J. 2003. Predicting interplanetary
765   magnetic field (IMF) propagation delay times using the minimum variance technique. *J. Geophys. Res*. **108**: 1026. DOI:
766   10.1029/2002JA009405.
767 Wik, M, Pirjola, R, Lundstedt, H, Viljanen, A, Wintoft, P, and Pulkkinen, A. 2009. Space weather events in July 1982 and October 2003 and
768   the effects of geomagnetically induced currents on Swedish technical systems. *Ann. Geophys*. **27**: 1775–1787. DOI: 10.5194/angeo-27-
769   1775-2009.
770 Wintoft, P, Wik, M, and Viljanen, A. 2015. Solar wind driven empirical forecast models of the time derivative of the ground magnetic field.
771   *J. Space Weather Space Clim*. **5**: A7. DOI: 10.1051/swsc/2015008.
772 Wintoft, P, Viljanen, A, and Wik, M. 2016. Extreme value analysis of the time derivative of the horizontal magnetic field and computed
773   electric field. *Ann. Geophys.* **34**: 485–491. DOI: 10.5194/angeo-34-485-2016.

Yamazaki, Y, and Maute, A. 2017. Sq and EEJ—A review on the daily variation of the geomagnetic field caused by ionospheric dynamo currents. *Space Science Rev*. **206**: 299–405*.* DOI: 10.1007/s11214-016-0282-z.

Zhang, XY, Zong, Q-G, Wang, YF, Zhang, H, Xie, L, Fu, SY, Yuan, C J, Yue, C, Yang, B, and Pu, ZY. 2010. ULF waves excited by negative/positive solar wind dynamic pressure impulses at geosynchronous orbit. *J. Geophys. Res.* **115**: A10221*.* DOI: 10.1029/2009JA015016.

Zhang, JJ, Wang, C, Sun, TR, Liu, CM, and Wang, KR. 2015. GIC due to storm sudden commencement in low-latitude high-voltage power network in China: Observation and simulation. *Space Weather*. **13**: 643–655*.* DOI:10.1002/2015SW001263.

Zhao, H, and Zong, Q-G. 2012. Seasonal and diurnal variation of geomagnetic activity: Russell-McPherron effect during different IMF polarity and/or extreme solar wind conditions, *J. Geophys. Res*. **117:** A11222*.* DOI: 10.1029/2012JA017845.

Zong, Q-G, Zhou, X-Z, Wang, YF, Li, X, Song, P, Baker, DN, Fritz, TA, Daly, PW, Dunlop, M, and Pedersen, A. 2009. Energetic electron response to ULF waves induced by interplanetary shocks in the outer radiation belt. *J. Geophys. Res*. **114**: A10204*.* DOI: 10.1029/2009JA014393.